

SEGMENTATION, REGISTRATION, AND TOPOGRAPHY-BASED  
FEATURE EXTRACTION FOR PLACENTAL MRI

by

James Huang

APPROVED BY SUPERVISORY COMMITTEE:

---

Dr. Baowei Fei, Chair

---

Dr. Kathleen Myers

---

Dr. Yichen Ding

Copyright 2022

James Huang

All Rights Reserved

SEGMENTATION, REGISTRATION, AND TOPOGRAPHY-BASED  
FEATURE EXTRACTION PLACENTAL MRI

by

JAMES HUANG, BS

THESIS

Presented to the Faculty of  
The University of Texas at Dallas  
in Partial Fulfillment  
of the Requirements  
for the Degree of

MASTER OF SCIENCE IN  
BIOMEDICAL ENGINEERING

THE UNIVERSITY OF TEXAS AT DALLAS

November 2022

## ACKNOWLEDGMENTS

I would like to express my deepest gratitude towards Dr. Baowei Fei for his continued guidance on this thesis work. I am extremely grateful to the members on the defense committee, Dr. Kathleen Myers and Dr. Yichen Ding for their help. Special thanks to Dr. Maysam Shahedi for his assistance and contributions on this thesis work. I am also thankful for the physicians at the University of Texas Southwestern Department of Radiology who have provided the data. Thanks should also go to all study participants for making this research study possible. Lastly, I'd like to give thanks to my friends and family for their support.

November 2022

# SEGMENTATION, REGISTRATION, AND TOPOGRAPHY-BASED FEATURE EXTRACTION FOR PRENATAL MRI

James Huang, MS  
The University of Texas at Dallas, 2022

Supervising Professor: Dr. Baowei Fei

During pregnancy, the placenta is a vital structure within the uterus which supplies the fetus with oxygen and nutrients while flushing its metabolic wastes out. A healthy pregnancy will see the placenta develop on the uterine wall towards the superior, left, or right sides and loosely attach to the uterus such that it will be naturally removed during birth. When abnormal placentation occurs, the placenta may grow in problematic locations, such as over the cervix, or attach too deeply into the uterine wall. Placental disorders occur in about 1 in 100 pregnancies, causing a multitude of complications from excessive bleeding after delivery to premature birth and usually require a postpartum hysterectomy. Clinical studies have emphasized the importance of proper placental development in gestational outcome, maternal and fetal health, as well as future wellbeing after delivery. However, the current clinical standard modality for the diagnosis of placental disorders is ultrasound (US) imaging, which suffers from a lack of the needed accuracy for analysis of placental shape, locale, volume, and other structural features. Magnetic resonance imaging (MRI) has shown in recent studies that its high soft tissue contrast and 3D viewpoint could potentially improve diagnosis of placental disorders in clinical obstetrics. Using uterine cavity and placental features extracted from prenatal MRI with computer-assisted analysis could

be the next step in advancing the speed and efficacy of identifying and treating pregnancy disorders. In this thesis work, we (1) propose a novel deep-learning based method for fully automatic segmentation of the placenta and uterine cavity labels from prenatal MR images and evaluate the model's performance, (2) address and seek to resolve a known issue associated with misalignment of interleaved slices in abdominal MRI through a realignment procedure based on demons registration, and (3) propose a new topography-based technique for visualizing placental surface features to provide a new point of observation for use in future computer-assisted diagnosis. Our studies seek to advance clinical prenatal MRI by building foundations for streamlined placental assessment and further establish MRI in clinical obstetrics alongside US as an imaging modality for diagnosing placental disorders.

## TABLE OF CONTENTS

## LIST OF FIGURES

<b>Figure 1.</b> High-level graphical abstract .....	2
<b>Figure 2.</b> Process to turn 3D MR image volumes into blocks of five slices each for inputs into the neural network .....	10
<b>Figure 3.</b> Convolutional neural network architecture .....	12
<b>Figure 4.</b> Training curves for segmentation models .....	15
<b>Figure 5.</b> Boxplots for segmentation performance on test data .....	16
<b>Figure 6.</b> 2D slices of predicted labels for four patient’s MR images .....	18
<b>Figure 7.</b> Superimposed 3D surfaces of predicted and ground truth labels .....	19
<b>Figure 8.</b> Poor segmentation performance case .....	20
<b>Figure 9.</b> Misalignment of even and odd slices of MR image volume due to motion .....	23
<b>Figure 10.</b> Process of interpolation and registration for alignment of even and odd slices in motion-corrupted prenatal MR images .....	26
<b>Figure 11.</b> Sagittal cross sections of MR image volumes pre- and post-registration .....	28
<b>Figure 12.</b> 3D surface visualizations of the pre- and post-registration placenta and uterine cavity labels .....	29
<b>Figure 13.</b> Intra-volume TRE plots between markers at adjacent slices for two selected anatomical landmarks .....	30
<b>Figure 14.</b> Polar topographic analysis approach .....	35
<b>Figure 15.</b> Topographic distance map for the maternal side surface points in a sample case .....	36
<b>Figure 16.</b> Planar topographic mapping definitions and sample intensity maps .....	38
<b>Figure 17.</b> Polar topographic feature maps from a normal case .....	39



<b>Figure 18.</b> Polar topographic feature maps from a PAS suspected case with postpartum hysterectomy.....	40
<b>Figure 19.</b> Planar topographic feature maps from a normal case .....	41
<b>Figure 20.</b> Artifacts of the polar topography mapping .....	42

## LIST OF TABLES

<b>Table 1.</b> Automatic segmentation performance on sagittal test dataset .....	17
<b>Table 2.</b> Automatic segmentation performance on axial test dataset.....	17

# **CHAPTER 1**

## **INTRODUCTION**

### **1.1 CLINICAL PROBLEM AND SIGNIFICANCE**

Normal growth and development of a human fetus is highly dependent on the concurrent normal development of the placenta. The placenta is a structure in the uterine cavity that is largely responsible for gestational outcome, providing essential functions during pregnancy including fetal support, nourishment, waste removal, and protection [1]. Abnormal placenta growth can have dramatic and lasting effects on the growth of the fetus as well as maternal health [2]. Placental dysfunction causes prematurity, pre-eclampsia, fetal growth restriction, and miscarriage or stillbirth, as well as “adult diseases” such as neurodevelopmental abnormalities [3] [4] [5] [6]. One of the most common placental complications is placenta accreta spectrum (PAS), which can lead to severe hemorrhaging, multisystem organ failure, hysterectomy, and even death due to the placenta not detaching normally from the uterus following delivery [7]. Therefore, detecting placental disorders early in the pregnancy is crucial to plan a proper course of action and minimize further issues down the line. Prenatal placental assessment is an integral part of the clinical gestational screening procedures that can be used to predict or detect conditions that result in potentially life-threatening complications during pregnancy and delivery [8] [9].

## 1.2 IMAGING FOR PLACENTAL EXAMINATION

Clinical imaging of the placenta gives insights into the location, shape, and volume of the placenta, all of which are crucial factors in the diagnosis of placental complications [10] [11]. Physicians also examine the interface between the placenta and uterus closely to diagnose disorders such as PAS. Currently, two-dimensional (2D) and three-dimensional (3D) ultrasound (US) are the clinical standards for imaging and diagnosing placental disorders. 2D-US carries several limitations, such as a poor ability to calculate placental structure and volume, as well as being burdensome for the physician to mentally reconstruct the placenta from 2D viewpoints [12]. The volume and thickness of the placenta is generally approximated from the longest diameter and the length of its shape as seen in the 2D images [13]. 3D-US has been adopted for better volumetric and structural assessment of the placenta and a combination of 3D-US with power Doppler US has seen success in the measurement of placental blood flow and vascularization [14] [15]. However, US techniques are still heavily limited by declines in image quality when the placental implantation site is towards the posterior and poor maternal body habits [16]. 2D-US and 3D-US both suffer from a limited field of view, making it difficult or impossible to view the entire placenta from a single viewpoint.

Magnetic resonance imaging (MRI) can compensate for these limitations, as it provides a 3D abdominal image with high soft-tissue contrast which is desirable for assessing placental, uterine, and fetal features in clinical obstetrics [17]. MRI provides an improvement in tissue resolution, a larger field of view, is less user-dependent, and is less affected by the habits of the mother and location of the placenta in the body [16] [18]. Studies have shown that MRI is better at imaging of the implantation interface between the placenta and uterine wall than US, which is

extremely important in diagnosing placental disorders like PAS [19]. Given the various advantages of MRI over US for certain characteristics of placental imaging and assessment, it follows that MRI could be used as a powerful supplementary imaging modality which can be used in combination with modern US techniques by obstetricians for placental disorder diagnosis and treatment planning.

### 1.3 PRIOR WORK ON PLACENTAL SEGMENTATION AND MRI REGISTRATION

Many researchers have been working towards the goal of accurate and fast segmentation of the placenta due to its importance in maternal health. The following is a brief introduction to the past and related work in placenta segmentation from medical images.

Han *et al.* utilized the U-Net for automatic placenta segmentation and modified it to be thinner and less computationally expensive using separable convolution [20]. Shahedi *et al.* proposed a minimally interactive semi-automatic segmentation tool which combined deep learning and region growing to segment the uterine cavity and placenta in MR images [21]. Shahedi *et al.* further improved their network and performed fully automatic segmentation of the uterine cavity and placenta in MR images using a 3D U-Net model [22] [23]. Looney *et al.* developed a two-pathway, hybrid convolutional neural network model using transfer learning to automatically segment the placenta [24]. Hu *et al.* applied a novel layer into the segmentation U-Net which was weighted by automated acoustic shadow detection to recognize artifacts specific to ultrasound [25]. Alansary *et al.* addressed the issue of motion corrupted prenatal MRI segmentation via a 3D multi-scale convolutional neural network and a conditional random field method [26]. Wang *et al.* developed a semi-automatic placenta segmentation tool called Slice-

Seg, which used slice-by-slice propagation to provide a minimally interactive segmentation of the placenta from sparse and motion-corrupted prenatal MRI [27]. More recently, Wang *et al.* proposed another deep learning-based semi-automatic segmentation method called DeepIGeoS, which combined automatic segmentations with user interactions through geodesic distance transforms to further refine segmentation results [28]. Zhang *et al.* designed a multi-region saliency-aware learning method for cross-domain *ex vivo* placenta image segmentation, which guides the translation between domains by enforcing attention and saliency consistency constraints [29]. Most recently, Zimmer *et al.* proposed a multi-task learning approach that combines the classification of placental location and semantic placenta segmentation in a fully convolutional neural network for ultrasound to achieve a high-quality segmentation with reduced image artifacts [30].

When considering the registration of MRI to correct for artifacts resulting from patient motion during imaging, there are several similar studies. The closest related work was a deformable slice-to-volume registration for motion correction of the fetal body and placenta in MRI proposed by Uus *et al* [31]. Guyader *et al.* examined pairwise and groupwise deformable registration solutions to the respiratory motion problem in lung MRI [32]. Menys *et al.* combined optical flow registration with an additional quantification of bowel motility during registration to correct respiratory motion in abdominal MRI [33]. An unsupervised deep learning solution for slice misalignment correction in cardiac MR imaging was proposed very recently by Chang *et al* [34]. To our best knowledge, topographical mapping techniques in the medical imaging field have only been loosely applied to visualization of the brain lesions [35] and knee cartilage interfaces [36].

## 1.4 OUTLINE OF THE PROPOSED WORK AND THE CONTRIBUTIONS

In this thesis work, we aimed to improve upon current methods for segmentation of the placenta and uterine cavity in prenatal MRI, presented a new method for motion correction in abdominal MRI, and introduced a topography-based avenue for visualization of the placenta for potential use in future diagnosis of placental disorders. The thesis can be divided into three studies, all of which, when viewed in conjunction, form a large section of a useful pipeline for prenatal placental assessment (see Figure 1).

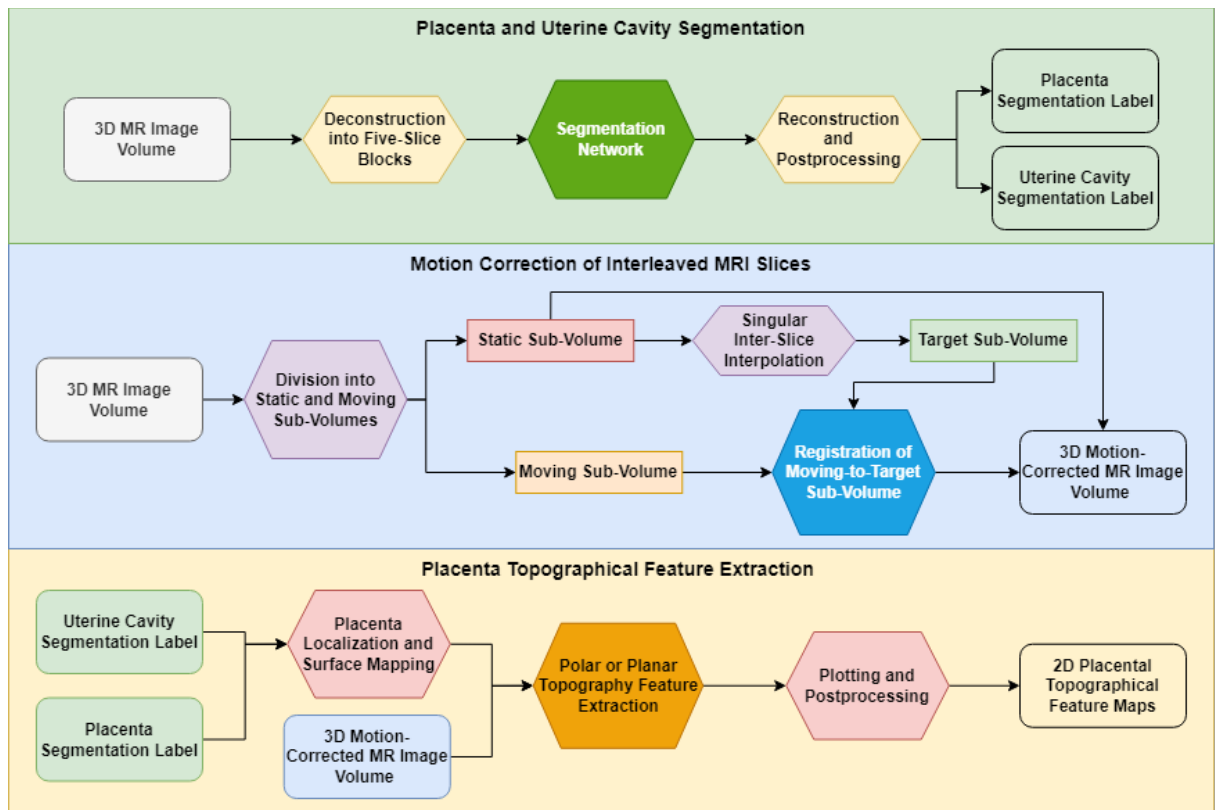


**Figure 1.** Graphical abstract detailing the proposed high-level segmentation, registration, and topography extraction pipeline for prenatal MR image analysis.

In Chapter 2, we designed a deep neural network to perform predictions of placenta and uterine cavity segmentations in prenatal MRI. We adapted the state-of-the-art U-Net 3+ model architecture to suit our data and achieved high test performances across multiple evaluation metrics. We extended our previous work on fully automatic segmentation of the placenta and uterine cavity with a 3D U-Net model [21] [23] [22].

In Chapter 3, we proposed a method to align abdominal MRI taken in an interleaved fashion that have been corrupted by respiratory motion via deformable image registration. The demons registration algorithm was applied alongside a sub-volume based registration target generation procedure to rectify misalignments between even and odd slices in the MRI volumes.

In Chapter 4, a topographical mapping method was proposed for viewing surface-level features of the placenta in two dimensions. The extracted features will be used in a future classification study to determine whether a patient requires a hysterectomy. Taken as a whole, this thesis work hopes to further MRI solutions for placental disorder diagnosis.



## **CHAPTER 2**

### **DEEP-LEARNING BASED AUTOMATIC SEGMENTATION OF THE PLACENTA AND UTERINE CAVITY ON PRENATAL MAGNETIC RESONANCE IMAGES**

#### **2.1 INTRODUCTION**

The current clinical standards for assessing placental health are two-dimensional (2D) and three-dimensional (3D) ultrasound (US), which places much of the strain on the physician to create placenta volumes in their mind and suffers from several limitations including approximation of the shape of the placenta, localizing features, and a small field of view. In recent years, magnetic resonance imaging (MRI) has shown potential benefits in analyzing pregnancy health. An addition of 3D magnetic resonance imaging (MRI) to clinical obstetrics may provide the improved soft tissue contrast and wider field of view needed to supplement placental investigation [17]. Studies have shown that MRI can highlight certain features such as intraplacental bands which have corresponded to abnormal placentation [37] [38].

This study is a continuation of our previous work in devising a fully automatic segmentation platform for delineating the placenta and uterine cavity in MRI of pregnant women. In the previous works, we demonstrated the advantages of end-to-end deep neural networks for placenta and uterus segmentation over semi-automatic methods and computerized algorithms [22] [23] [21] [27] [39]. Deep learning brings the advantages of speed of computation time and improved segmentation accuracy of medical images [40]. In this study, our objective is to present a fully automatic deep learning segmentation model for fast, accurate, and repeatable

3D segmentation of the placenta and uterine cavity in sagittal and axial T2-weighted MRI of pregnant women with and without placental complications. We used a 3D U-Net 3+ architecture to implement our end-to-end prediction model and achieved an average Dice similarity coefficient (DSC) of 95.3% for uterine cavity and of 87.7% for placenta on the sagittal dataset and an average DSC of 91.8% for uterine cavity and of 82.7% for placenta on the axial dataset. A clinical obstetrics application of the automatic segmentation method can provide a powerful analytical tool to assess the risk of pregnant women with placenta accreta spectrum.

## **2.2 METHODS AND MATERIALS**

### **2.2.1 Data**

We used two datasets for this study, one with 101 sagittal MR images, of which all the patients imaged were also part of the second dataset, which contained 241 MR images taken in the axial direction. The sagittal dataset contained 101 T2-weighted MR image volumes of the uterus obtained from 101 normal pregnant women. Each of the image volumes had between 27 and 80 2D sagittal slices, with each slice sized at 256 x 256 pixels. The MR images were taken in an interleaved fashion, with a spacing of either 5 mm or 6 mm between neighboring slices. Corresponding physical sizes of the image pixels ranged from 1.172 x 1.172 mm<sup>2</sup> to 1.758 x 1.758 mm<sup>2</sup>. The axial dataset contained 241 T2-weighted MR image volumes of the uterus of 241 pregnant women with suspicion of PAS or other placental abnormalities. 88 of the 241 women in this dataset underwent a hysterectomy procedure sometime after imaging. Each image volume contained between 28 and 62 2D axial slices spaced 7 mm apart. The slices were sized at

256 x 256 pixels except for three cases with smaller sizes. The physical sizes of the image pixels in the axial dataset ranged from 1.051 x 1.051 mm<sup>2</sup> to 1.953 x 1.953 mm<sup>2</sup>. For both datasets, manually segmented labels of the uterine cavity and the placenta were provided by an expert radiologist.

## 2.2.2 Data preparation and preprocessing

To prepare the data, any cases in the axial dataset with MR image slice sizes of less than 256 x 256 pixels were first zero-padded across the entire volume to be 256 x 256 pixels. Following this, the data preparation and preprocessing steps for the sagittal and axial datasets were the same. The MR image volumes and labels were cropped along the imaging axis based on the manual segmentations to contain only those slices containing uterine cavity. This step narrowed the minimum and maximum number of MR image volume slices in the sagittal dataset from (26 to 80) to (24 to 61). Similarly, the range of the slices in the axial dataset was reduced from (28 to 62) to (24 to 61). A 2D median filter with a kernel size of 3 x 3 was applied to each image slice to reduce image noise. Additionally, intensity-level slicing and normalization were applied to the MR image volumes according to the following equation:

$$\hat{I}_i(x, y, z) = \begin{cases} 0 & \text{if } I_i(x, y, z) < p_5(I_i) \\ 1 & \text{if } I_i(x, y, z) > p_{99}(I_i) \\ \frac{I_i(x, y, z) - p_5(I_i)}{p_{99}(I_i) - p_5(I_i)} & \text{otherwise} \end{cases} \quad (1)$$

where  $I_i(x, y, z)$  represents the original intensity of a given voxel in an image volume,  $\hat{I}_i(x, y, z)$  represents the new intensity of the voxel, and  $p_5(I_i)$  and  $p_{99}(I_i)$  represent the 5<sup>th</sup> and 99<sup>th</sup> intensity percentiles across the image volume, respectively.

Because the placenta was always entirely within the uterine cavity, there was a complete overlap between the manual segmentation label of the placenta and the uterine cavity. To convert the label volumes into one-hot encoded tensors, the placenta label was subtracted from the uterine cavity label to create a new uterus channel without the intersection. The placenta channel was not modified, and the background channel was generated by inverting the original uterine cavity label. Finally, the channels were stacked along the fourth axis to create image volumes of shape  $256 \times 256 \times N \times 3$ . To keep the network inputs homogeneous, blocks of five consecutive slices were extracted from the training image volumes, with a separate  $256 \times 256 \times 5$  sized contiguous block for each possible position within the volume for a total of  $N-4$  training cases per image. The image blocking procedure is detailed in Figure 2, where the identification for each block extracted from an MR image volume is given as  $B_i^l$ , with  $i$  representing the number of the initial slice of the block as part of the volume sequence, and  $l$  representing the number of the last slice in the block.

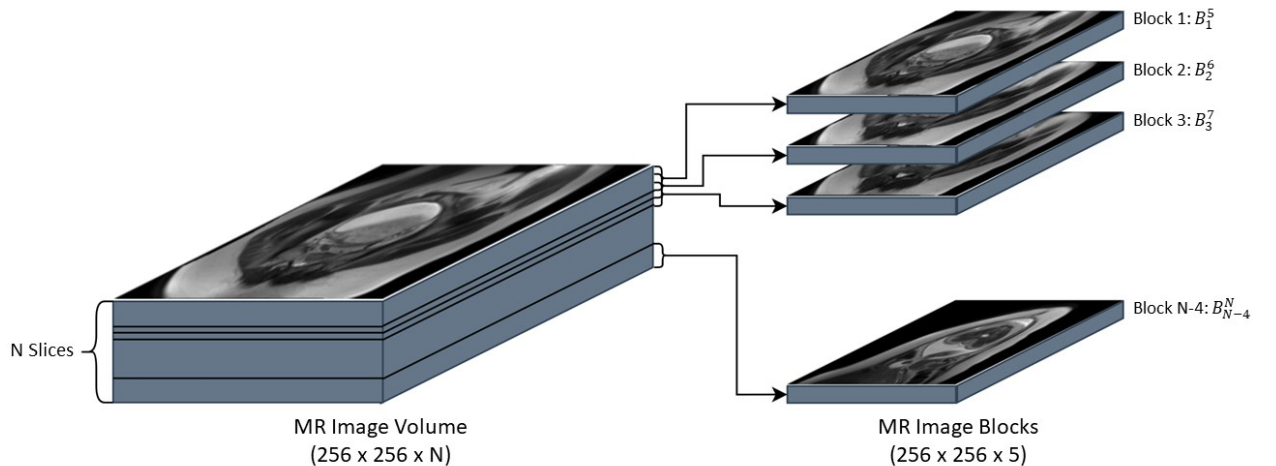


**Figure 2.** Process to turn 3D MR image volumes into blocks of five slices each for inputs into the neural network.

Both datasets were divided randomly using a 70-10-20 training, validation, testing split. The 101 sagittal image data were randomly split into groups of 71 training, 10 validation, and 20 testing images. The 241 axial image data gave 169 training, 24 validation, and 48 testing images. When feeding image blocks into the network, we applied a simple data augmentation of left-right flipping across the block at a 50% chance.

### 2.2.3 Neural network architecture

For the automatic segmentation task, we used the state-of-the-art U-Net 3+ architecture proposed by [41], which makes an improvement on the normal U-Net and U-Net++ by employing full-scale skip connections to increase positional and boundary awareness in segmentation while keeping the model size relatively small. U-Net 3+ adds skip connections from each encoder layer to each decoder layer of equal or deeper depth, as well as intra-skip connections between all decoder layers. These full-scale skip connections are used to integrate low-level details with high-level positional information from feature maps in different scales, which is where the U-Net and U-Net++ fall short by failing to explicitly learn positional and bounding details from organs in segmentation tasks. The U-Net 3+ combines this holistic hierarchical data from the low- and high-level features of the image via max pooling each low-level encoded layer with a larger resolution than the output decoder layer and bilinear up-sampling each high-level encoded layer with a smaller resolution than the output decoder layer [41]. Huang *et al.* also proposed a module called a classification-guided module (CGM), which applies an extra classification task for predicting whether the input image has organ or not to reduce the number of false-positives, but this was not utilized in our work due to the preprocessing steps making the CGM unnecessary.

We hoped the incorporation of the U-Net 3+ would yield improvements in segmentation performance as compared to our previous U-Net model. The original U-Net 3+ proposed by Huang *et al.* is a 2D network with five resolution levels. We modified the U-Net 3+ to accept 3D inputs of size  $256 \times 256 \times 5 \times 1$  and output segmentation predictions of size  $256 \times 256 \times 5 \times 3$  with the background, placenta, and uterine cavity as the three channels. Additionally, we reduced the number of resolution levels from five to four to greatly lighten the memory load. The convolutional neural network (CNN) architecture is detailed in Figure 3. As an example of data flow in the 3D U-Net 3+, the decoder  $D2$  as shown in Figure 3 was fed through the concatenation of all four encoder layer outputs. Encoder layer  $E1$ , having a two times larger resolution than  $D2$ , was max pooled by a factor of two and passed through 64 filters. Encoder layer  $E2$  with the same resolution as  $D2$  was simply filtered and concatenated. Encoder layer outputs  $E3$  and  $E4$  were up-sampled using bilinear interpolation at two and four times the resolutions, respectively, before filtering and concatenation. The filters at the decoder input at each encoder scale provide crucial learning parameters for enhancing the organ segmentation performance of the U-Net 3+ model.

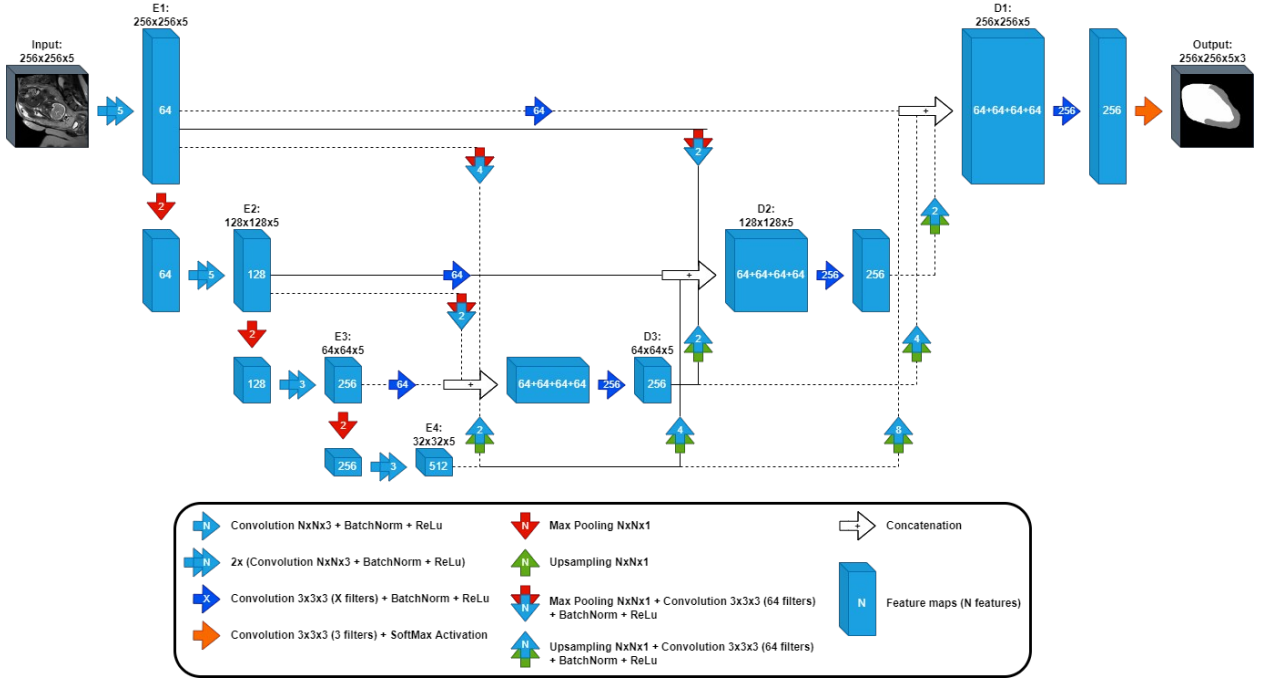


**Figure 3.** Convolutional neural network architecture (3D U-Net 3+). The network accepts inputs of size 256x256x5 and outputs channels corresponding to background, placenta, and uterine cavity for each voxel for a total output size of 256x256x5x3. *E1*, *E2*, *E3*, and *E4* refer to encoder layers 1, 2, 3, and 4, respectively. *D3*, *D2*, and *D1* refer to decoder layers 3, 2, and 1, respectively.

The chosen hybrid loss function was given as:

$$L = \alpha L_{pl} + \beta L_{ut} \quad (2)$$

where  $L_{pl}$  was the placenta label Dice similarity coefficient (DSC) and  $L_{ut}$  was the uterine cavity label DSC. The loss weights were chosen as  $\alpha = 0.6$  and  $\beta = 0.4$  to give slightly greater weight to the placenta.

### 2.2.4 Implementation details

The 3D U-Net 3+ architecture was written in Python using TensorFlow and Keras. We trained the network for up to 300 epochs and saved weights based on best validation loss. Our machine was a high-performance computer with four NVIDIA RTX A6000 GPUs, each with 48 GB of memory. Due to the large size of the network, the batch size was initially restricted to eight 3D input blocks on one GPU. We artificially expanded this to 32 blocks per batch by employing the TensorFlow mirrored distribution strategy to duplicate the model onto the four available GPUs. Training was done using the Adam optimizer with an initial learning rate of  $1e-4$ .

### 2.2.5 Postprocessing

Using the 20 testing images from the sagittal dataset and the 48 from the axial dataset, each testing image set was fed into the trained network with a single eight-slice block at a time with a four-slice overlap with the next block. The blocks were also flipped from left-right and separate predictions were made on the original and mirrored blocks. The mirrored predicted label was flipped again and was averaged with the original predicted label. With a SoftMax output layer, the network output probabilities for each voxel across the three channels summing to 1. All calculated voxel probabilities were added to an empty array with the size of the label volume with block overlap, which was finally collapsed into a ternary output label using TensorFlow's *argmax* function, which collapses a tensor along a specified axis by replacing the values across the axis with the index of the largest value.



Resultant predicted uterine cavity and placenta segmentation labels were further postprocessed in MATLAB using a four-step segmentation smoothing and filling process proposed by [42]. First, a 3D erode operator was applied to the predicted labels with a cubic structuring element of size 3 x 3 x 3 to remove small protrusions from the label. Next, the islands in the label volumes were removed by keeping only the largest 26-connected component of the labels. In the third step, the labels were dilated using a cubic structuring element of size 3 x 3 x 3. Lastly, the holes, or regions in the segmentations labeled as 0 unreachable from the surface of the volume, were filled in.

### 2.2.6 Evaluation

We compared the predicted labels to the manually segmented labels using several error metrics: Dice similarity coefficient (DSC), Hausdorff distance (HD), signed volume difference (VD), and percent signed volume difference. The Dice similarity coefficient can be calculated as follows:

$$Dice = \frac{(2 * Area\ of\ Overlap)}{Total\ pixels\ combined} \quad (3)$$

The Hausdorff distance is calculated as the greatest of all the distances from a point in one image to the closest point of the same class in the other image [43]. The volume difference and percent volume difference can be calculated as follows:

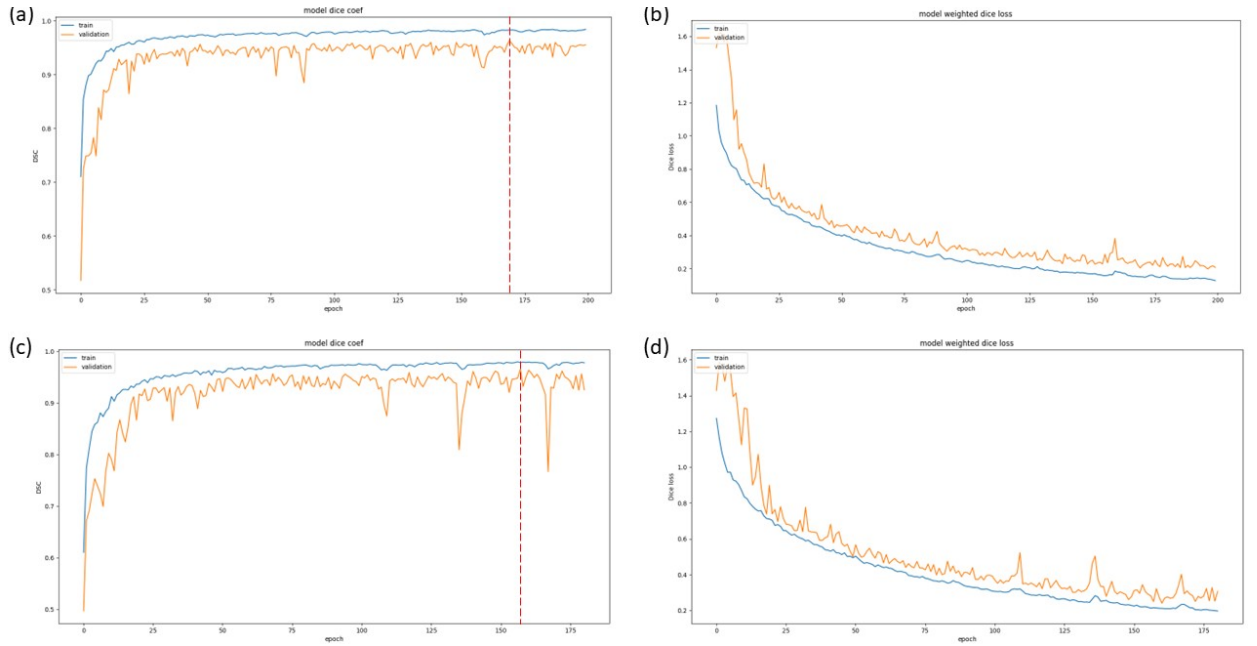
$$\Delta V = V_{pred} - V_{ref} \quad (4)$$

$$\Delta \%V = \frac{V_{pred} - V_{ref}}{V_{ref}} * 100 \quad (5)$$

where  $\Delta V$  represents the raw volume difference scaled to the real world using the corresponding physical sizes of the image pixels,  $V_{pred}$  represents the total 3D volume of the uterine cavity or placenta predicted label, and  $V_{ref}$  represents the total 3D volume of the uterine cavity or placenta ground truth label.

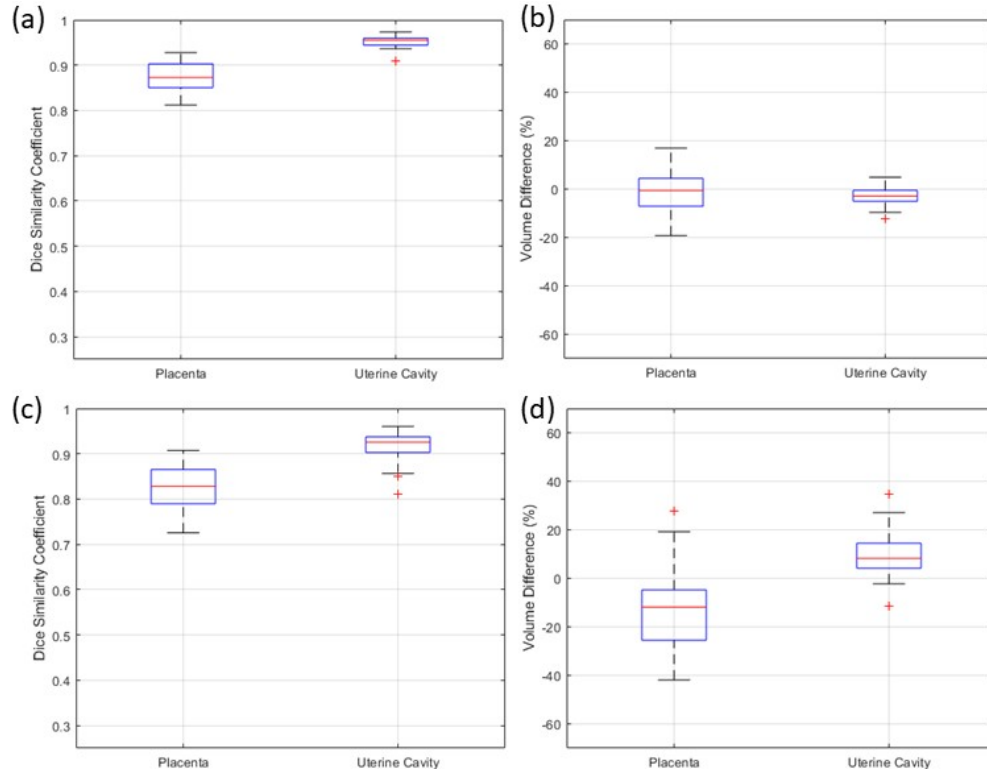
## 2.3 RESULTS

Figure 4 shows the training and validation curves for the sagittal and axial 3D U-Net 3+ models. The best validation dice score was achieved at epoch 169 for the sagittal model and epoch 157 for the axial model.



**Figure 4.** Training curves given as a) overall dice coefficient of sagittal model, b) weighted dice loss of sagittal model, c) overall dice coefficient of axial model, and d) weighted dice loss of axial model. Red dotted lines indicate the epoch at which the best training weights were achieved.

The held-out test data of the sagittal and axial datasets were segmented using the best training models for each dataset. The end-to-end process of forming a prediction label on an entire image volume, including all postprocessing steps, took approximately one minute on average. Figure 5 displays a boxplot for the DSC and percent volume difference on all test data segmentations as compared to the ground truth labels for the sagittal and axial models.



**Figure 5.** Boxplots for placenta and uterine cavity segmentation performance represented as a) DSC for sagittal model, b) percent volume difference for sagittal model, c) DSC for axial model, and d) percent volume difference for axial model. Sagittal model was evaluated on held-out test data with  $n=20$  and axial model was evaluated on held-out test data with  $n=48$ .

In the sagittal dataset, we achieved a DSC of  $0.953 \pm 0.014$  and  $0.877 \pm 0.031$  for the uterine cavity and placenta, respectively. In the axial dataset, we achieved a DSC of  $0.918 \pm 0.033$  and  $0.827 \pm 0.051$  for the uterine cavity and placenta. Tables 1 and 2 show the full results of testing the best models on the sagittal and axial data using the four selected error metrics. We trained our old 3D U-Net network on the data with the same hyperparameters and postprocessing steps to compare performances. Each evaluation metric is a comparison between the predicted label and manually segmented label from the same MR image.

**Table 1.** Automatic segmentation performance of the proposed 3D U-Net 3+ network and previous 3D U-Net network on the 20 test images of the sagittal MRI dataset. Error metrics are presented as mean  $\pm$  std for the placenta and uterine cavity labels.

	Placenta				Uterine cavity			
	DSC (%)	HD (mm)	VD (cm <sup>3</sup> )	VD (%)	DSC (%)	HD (mm)	VD (cm <sup>3</sup> )	VD (%)
<b>U-Net 3+ (new)</b>	$87.7 \pm 3.1$	$20.6 \pm 10.6$	$-16.6 \pm 109$	$-1.24 \pm 9.25$	$95.3 \pm 1.4$	$13.0 \pm 11.4$	$-146 \pm 226$	$-2.91 \pm 4.50$
<b>U-Net (previous)</b>	$83.4 \pm 5.7$	$24.7 \pm 21.5$	$-23.4 \pm 151$	$-1.75 \pm 12.8$	$88.6 \pm 3.4$	$25.2 \pm 10.1$	$-172 \pm 419$	$-3.43 \pm 8.34$

**Table 2.** Automatic segmentation performance of the proposed 3D U-Net 3+ network and previous 3D U-Net network on the 48 test images of the axial MRI dataset with  $n=16$  for number of hysterectomy patients and  $n=32$  for non-hysterectomy patients. Error metrics are presented as mean  $\pm$  std for the placenta and uterine cavity labels.

	Placenta				Uterine cavity			
	DSC (%)	HD (mm)	VD (cm <sup>3</sup> )	VD (%)	DSC (%)	HD (mm)	VD (cm <sup>3</sup> )	VD (%)
<b>U-Net 3+ (new)</b>	82.7 ± 5.1	19.3 ± 9.2	-90.5 ± 159	-11.2 ± 17.9	91.8 ± 3.3	17.2 ± 14.2	374 ± 337	10.3 ± 9.3
<b>U-Net (previous)</b>	81.0 ± 7.2	25.5 ± 20	-84.2 ± 207	-10.4 ± 23.3	87.2 ± 5.6	26.1 ± 9.8	-391 ± 433	-10.8 ± 12

Sample slices of predicted labels of the placenta and uterine cavity for four cases overlaid onto the original test image slices are shown in Figure 6. Another four example cases of 3D surface overlaps of predicted placenta and uterine cavity labels with the ground truth labels are shown in Figure 7.

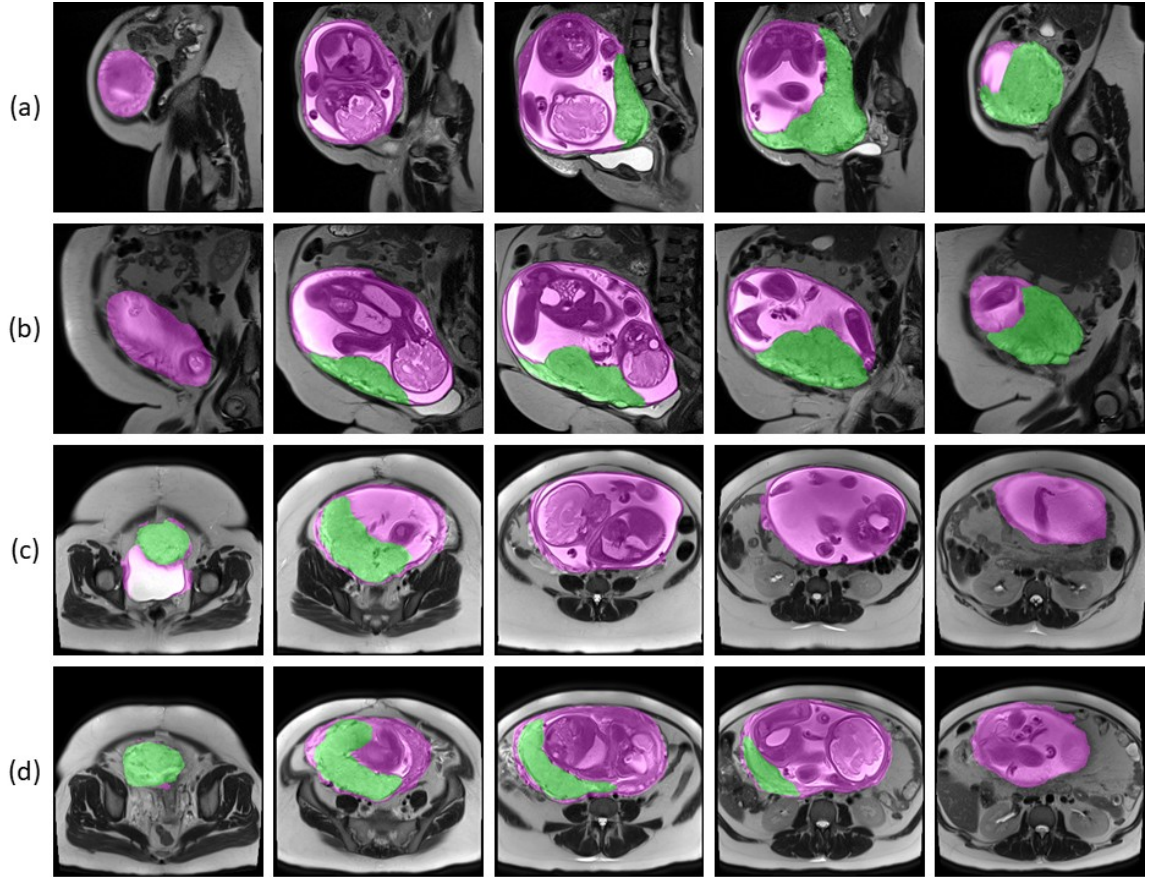


**Figure 6.** Predicted labels for four patient's MR images (rows a, b, c, and d) with five selected 2D slices across the volume for each. a) and b) are sagittal images. c) and d) are axial images. Labels are overlaid over the original image slices in magenta and green for uterine cavity and placenta, respectively.

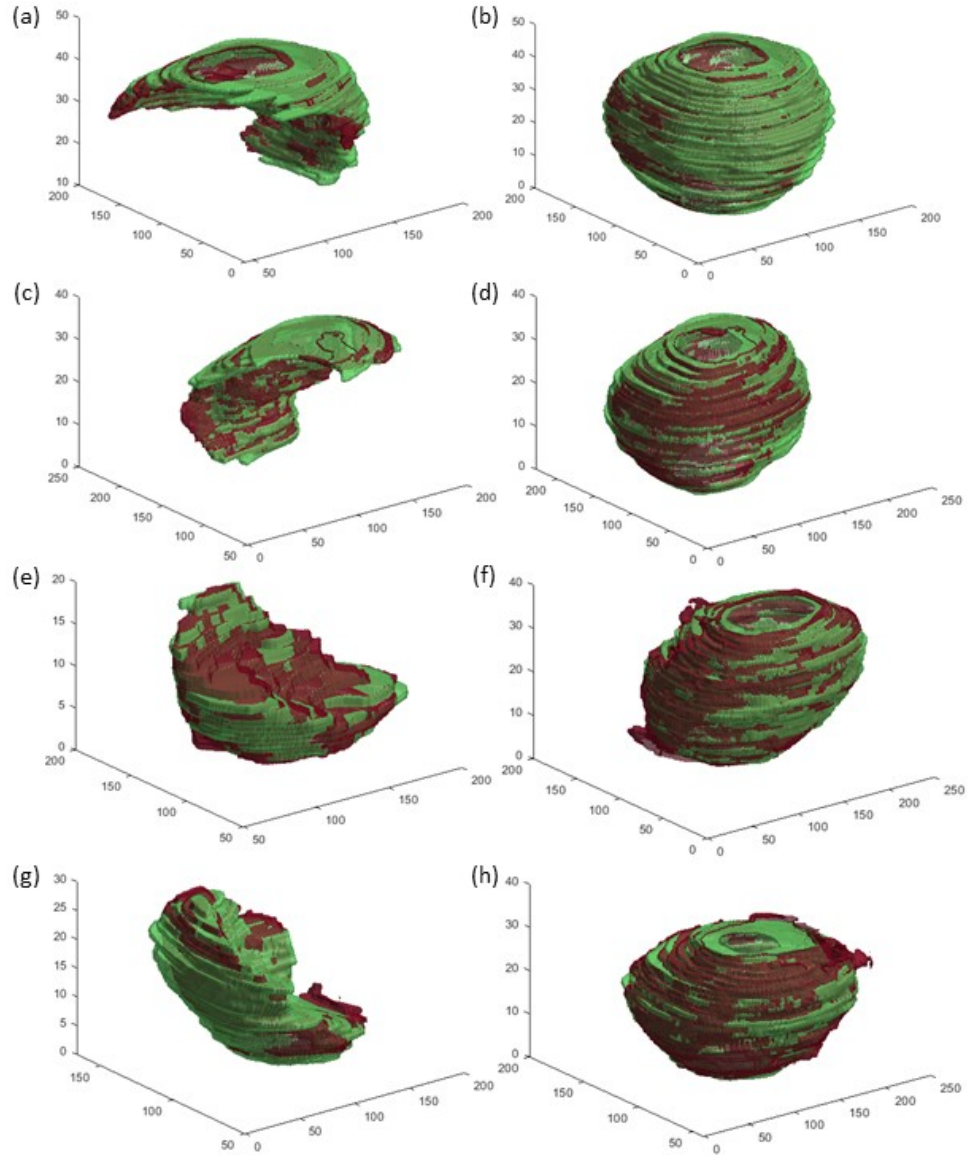


**Figure 7.** Superimposed 3D surfaces of predicted placenta (left column) and uterine cavity (right column) segmentation labels and ground truth labels for four test cases, with each row of images from the same patient. a), b), c) and d) are sagittal image cases. e), f), g), and h) are axial image cases. Predicted labels are shown in maroon and ground truths are shown in green.

## 2.4 DISCUSSION AND CONCLUSIONS

### 2.4.1 Discussion

On the sagittal dataset consisting of MR images of only normal pregnancies, we achieved an improvement of 4.3% in dice score on the placenta (83.4% to 87.7%) and 6.7% on the uterine cavity (88.6% to 95.3%). The 3D U-Net 3+ model demonstrated superior performance to the 3D U-Net model for all evaluation metrics. The network seemed to predict the uterine cavity and placenta labels quite accurately, with high average DSC and low average VD for both. On the axial dataset consisting of MR images of both normal and abnormal pregnancies, we achieved an improvement of 1.7% in dice score on the placenta (81.0% to 82.7%) and 4.6% on the uterine cavity (87.2% to 91.8%). In contrast with the sagittal dataset, the network under-segmented the placenta but tended towards over-segmentation of the uterine cavity. Figure 8 depicts an example of a poor segmentation in an axial image case.

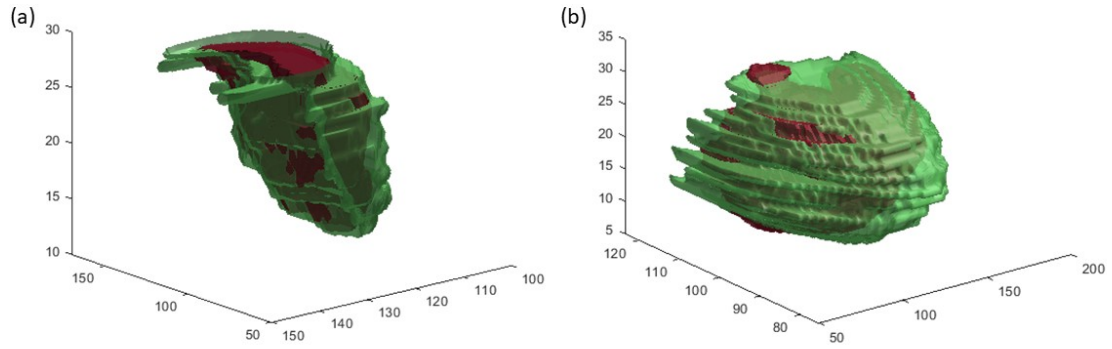


**Figure 8.** Poor segmentation performance case in an axial image, shown as superimposed 3D surfaces of predicted and ground truth labels of the a) placenta and b) uterine cavity. Predicted labels are shown in maroon and ground truths are shown in green.

In Figure 8, the network severely under-segmented both the placenta and the uterine cavity. Because over a third of the axial dataset consisted of patients who eventually underwent a hysterectomy, the underperformance of the axial network compared to the sagittal network could possibly be attributed to the large variability in placenta shape between patients with placental complications.

Training of the deep neural network was hindered by memory limitations and the amount of data. With the goal of 3D segmentation of the placenta and uterine cavity in mind, the network accepted image blocks as inputs of size 256 x 256 x 5. Allowing for training on larger input blocks than five slices could further improve segmentation performance by widening the field of view. However, with the size of the 3D U-Net 3+ model and number of parameters, the amount of available video memory limited the size of the 3D blocks and posed a challenge for training optimally. As with other deep learning-based medical image segmentation tasks, the network would benefit from additional data.



### 2.4.2 Conclusions

We proposed a new 3D U-Net 3+ architecture which is able to automatically segment the placenta and uterine cavity on whole MR image volumes with relatively high accuracy in a rapid way. Performance of automatic segmentation algorithms seems to still be limited heavily by the amount of data, especially in abnormal placenta cases, which can cause large inter-patient variability in uterus and placenta shapes. However, the results have been promising in terms of comparative performance to current MRI segmentation methods on the axial slices and brings us closer to effective computer-aided diagnosis of maternal and fetal health in clinical obstetrics. In the future, we plan to provide specific, quantifiable insights on the advantages or disadvantages of sagittal MRI over axial MRI for prenatal imaging, as well as apply additional augmentations, post-processing techniques, and binning methods that may improve upon our current segmentation results.

# **CHAPTER 3**

## **DEFORMABLE REGISTRATION FOR ADJACENT-SLICE MOTION CORRECTION**

### **IN PRENATAL MAGNETIC RESONANCE IMAGES**

#### **3.1 INTRODUCTION**

Abdominal magnetic resonance imaging (MRI) has been used extensively for decades to diagnose diseases and complications with the liver, pancreas, kidneys, and other organs due to its ability to image soft tissues with high contrast [17] [44]. However, one of the major issues with abdominal MRI is the long, non-simultaneous imaging time, which calls attention to respiration and additional patient motion in between acquisitions as factors impacting image quality. These confounding effects of respiration and motion show up in the form of misaligned even and odd slices and other artifacts in the constructed image volume when taken in the common interleaved acquisition scheme [32] [45]. MRI scans are usually taken while the patient holds their breath to reduce the degree of motion corruption, but for a normal healthy patient, breath holding for the entire imaging duration is difficult, even more so for a pregnant patient [46].

Correcting this misalignment between adjacent slices in magnetic resonance (MR) image volumes (see Figure 9) is the subject of many recently published and ongoing studies involving intra-image registration, including optical flow, three-dimensional (3D) recurrent neural networks for alignment, and registration using structural neighborhood descriptors [33] [34] [47].

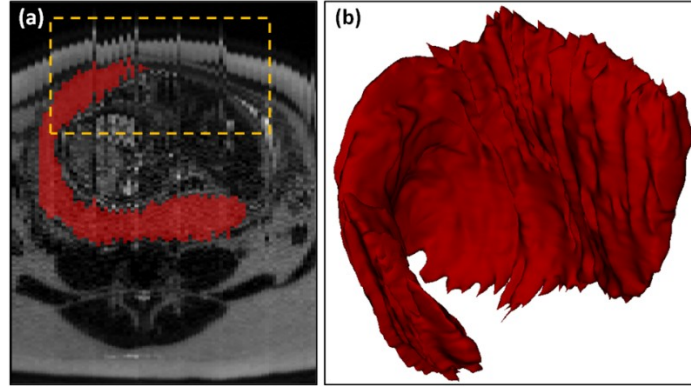


**Figure 9.** Misalignment of even and odd slices of MR image volume due to motion. a) depicts artifacts in a sagittal cross section of an axial MR image and b) shows the 3D surface of the manually segmented placenta label.

In this study, we proposed a minimally destructive method for rectifying even-odd slice misalignment in prenatal MR images using non-rigid registration. Whereas contemporary solutions for intra-image registration in abdominal MRI perform relatively well for slice alignment [33] [32], they engage in pairwise registration, which deforms both images in comparison to an abstract reference space “in between” the original images, called the mid-space [48] [49] [50] [51]. This lack of original shape preservation does not translate well into prenatal imaging, where the shape of the placenta is potentially crucial for diagnosis of complications [9] [52] [38]. Our work only applied deformable registration to one of the even or odd sub-volumes and does so by creating an artificial target sub-volume through interpolation, leaving the other sub-volume completely untouched. We hoped to improve the overall MR image quality, reducing artifacts and smoothing organ surfaces such that we would see a noise reduction when computing the topography maps of the placenta in Chapter 4 of this thesis work.

## **3.2 METHODS AND MATERIALS**

### **3.2.1 Data**

Our dataset for this study was composed of 241 T2-weighted MR image volumes of the uterus from 241 pregnant women. In the dataset, there were normal cases as well as patients with placenta accreta spectrum (PAS) or other placental complications, some of which later underwent postpartum hysterectomy. The data collection process and the research study were done observing IRB approved protocols. Each volume contained between 28 and 62 2D axial slices spaced 7 mm apart. The slices were 256 x 256 pixels in size except for three cases with sizes 208 x 208 pixels and 212 x 212 pixels. The physical sizes of the image pixels in the dataset ranged from 1.051 x 1.051 x 7 mm<sup>2</sup> to 1.953 x 1.953 x 7 mm<sup>2</sup>. Manually segmented labels for the placenta and uterine cavity in each MR image volume were given by an expert radiologist.

### **3.2.2 Interpolation**

The approach taken to address the misalignment between even- and odd-numbered slices in MR imaging was a two-step process consisting of an interpolation step and a deformable registration step. In the interpolation step, each MR image volume, along with its placenta and uterine cavity segmentation labels, was first divided into an even and an odd sub-volume by extracting every two image and label slices, starting from the first slice to create the odd-numbered volume, and starting from the second slice to create the even-numbered sub-volume. To minimize the degrees of deformations imposed onto the image and to retain image fidelity, only one of the even and odd volumes was designated as the static, or fixed volume, while deformations were only applied to the floating, or moving sub-volume. The fixed sub-volume

was chosen to be the volume with the positionally lowest uterine cavity center of mass, or the volume imaged at the time of greater exhalation. The reasoning for this was that deformation field singularities, or regions where the resultant registration deformation field would not be bijective, would mostly occur in image regions outside of the patient when the deformation field reflects compressing the patient's abdominal region [53]. Because the MR images were acquired along the transverse axis with the patient in the supine position, the fixed sub-volume was the volume of which the uterine cavity center of mass was closer to the anatomical posterior position. The second sub-volume was selected as the moving volume to be registered.

A target image volume was generated by performing image up-sampling across the transverse axis of the fixed image volume. Using the MATLAB function *meshgrid*, a 3D-grid of coordinates with double the number of slices of the fixed volume minus one was created, keeping the overall image dimensions the same but introducing a new slice at each halfway point between slices. The fixed volume was then interpolated with spline interpolation to the grid using the function *interp3*. The interpolated slices at each halfway point were taken as a new target image volume. The target image volume was sharpened using unsharp masking with a Gaussian function radius of 1.5 and a sharpening ratio of 150% to better highlight edge information. The process of up-sampling a fixed odd-numbered volume and extracting the target volume is shown in Figure 10.



**Figure 10.** Process of interpolation and registration for alignment of even and odd slices in motion-corrupted prenatal MR images.

### 3.2.3 Deformable registration

The misalignment of the adjacent slices in the MR image volume could be attributed to respiration during image acquisition, and to a lesser degree, small patient movements. To correct the misalignment, we adopted the demons algorithm for automatic non-rigid image registration. The demons registration is based on the optical flow equation used to find small, local deformations in temporal sequences of images [54]. The algorithm uses a diffusion model in

which each point along a contour of a moving image is assigned a demon that applies a local force to push the moving image either inwards or outwards, towards the boundary of some given object [55] [56] [54]. For a given point in the static image  $S$  with intensity  $I_s$  and a given point in the moving image  $M$  with intensity  $I_m$ , the improved optical flow equation proposed by [57] for calculating the estimated displacement required  $\vec{u}$  is given as:

$$\vec{u} = (I_m - I_s) * \vec{\nabla} I_s \quad (6)$$

where  $\nabla$  is the gradient operator and  $\alpha$  is a normalization factor used to control the demons force strength at each iteration adaptively [58] [59]. The demons algorithm calculates the optical flow equation in (6), or estimated displacement at each iteration and attempts to minimize a global energy function with respect to  $\vec{u}$ . In each iteration, the displacement vector field (DVF) was regularized using a Gaussian filter to enforce a smooth and realistic deformations to avoid folding and singularities [57] [54]. The energy function was optimized until convergence and can be described as follows:

$$E(\vec{u}) = (I_m - I_s + \vec{u} \cdot \vec{\nabla} I_s)^2 + \alpha^2 (I_m - I_s)^2 \cdot \vec{u}^2 \quad (7)$$

where each term in (7) is the same as described in (6) and  $E(\vec{u})$  represents the energy of a given displacement field. In this study, the MRI data was not a temporal sequence, and therefore it would be unreasonable to assume small deformations. The popular pyramidal coarse-to-fine multiresolution method proposed by [60] performs multiple stages of DVF optimization at successively higher resolutions, where the converged solution at each stage is passed on to the next as the new starting solution [57]. This reduces the negative effects of large deformations on the final registered image. As shown in Figure 10, our demons registration process used three

stages at resolutions of  $64 \times 64$ ,  $128 \times 128$ , and  $256 \times 256$  with 100, 50, and 25 iterations, respectively to guarantee convergence.

After the DVF mapping the moving image volume to the target volume was calculated, the moving image volume and its corresponding placenta and uterine cavity labels were deformed using the *imwarp* function. The final image and segmentation label volumes were reconstructed by interleaving the static and registered volumes together.

### **3.3 RESULTS**

The center sagittal slice of the MR image volumes was taken to showcase a degree of improvement in adjacent slice alignment following the registration step. Two examples of the mid-slice of the original and registered MR image volumes taken along the sagittal plane are shown in Figure 11. Additionally, the surfaces of the binary masks for the placenta and uterine cavity resulting from registration were displayed from a 3D perspective. In Figure 12, two comparative registration results are shown through the 3D surface visualizations of the pre- and post-registration placenta and uterine cavity labels.



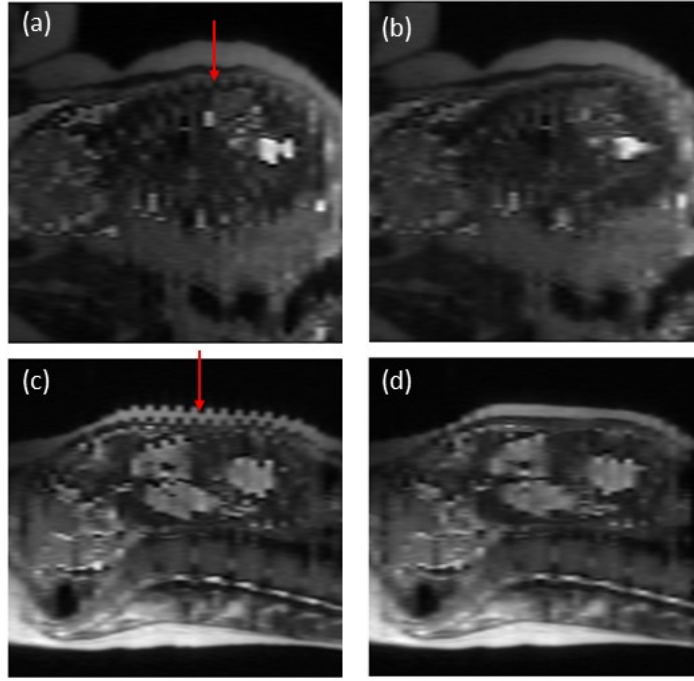


**Figure 11.** Sagittal cross section of MR image volumes pre- and post-registration for two patient cases with severe interleaved slice misalignment. A) and b) are pre- and post-registration results, respectively, for case 1. C) and d) are pre- and post-registration results, respectively, for case 2.

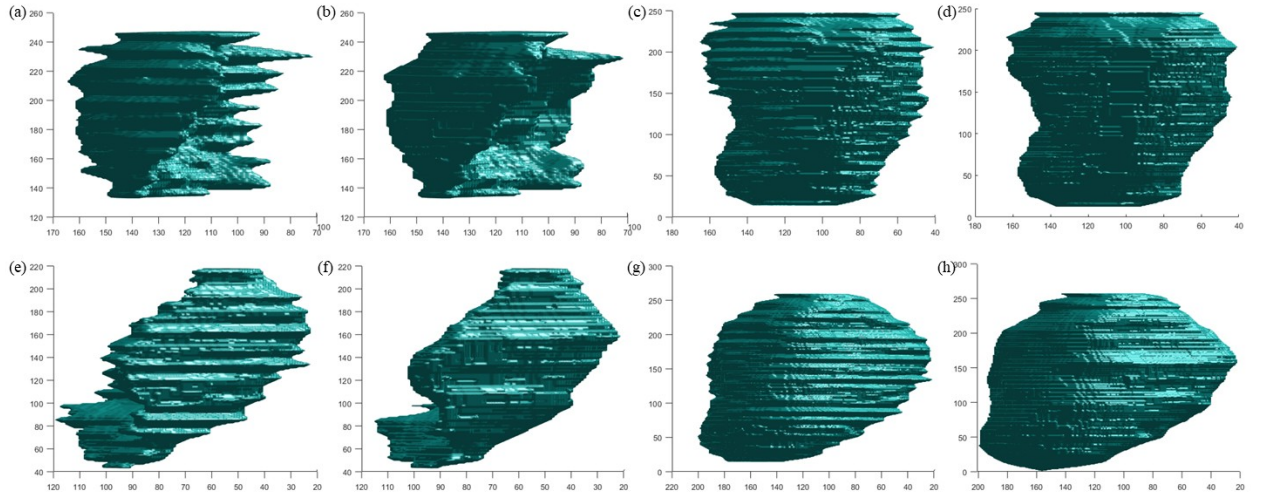


**Figure 12.** 3D surface visualizations of the pre- and post-registration placenta and uterine cavity labels for two patient cases. Case 1 displays a) pre- and b) post-

registration placenta labels and c) pre- and d) post-registration uterine cavity labels.

Case 2 displays e) pre- and f) post-registration placenta labels and g) pre- and h) post-registration uterine cavity labels.

Target registration error (TRE) is generally used for evaluating registration of temporal sequences by manually placing several markers at the same set of locations of anatomical landmarks in two images and finding the inter-image distance between the corresponding markers. In this study, the distances between markers in adjacent slices of the same image were computed using ImageJ, with targets chosen at less exact anatomical landmarks, such as “central-uppermost point on the border of the uterine cavity.” Figure 13 displays an adjacent-slice distance plot at two selected anatomical landmarks for a sample registration.

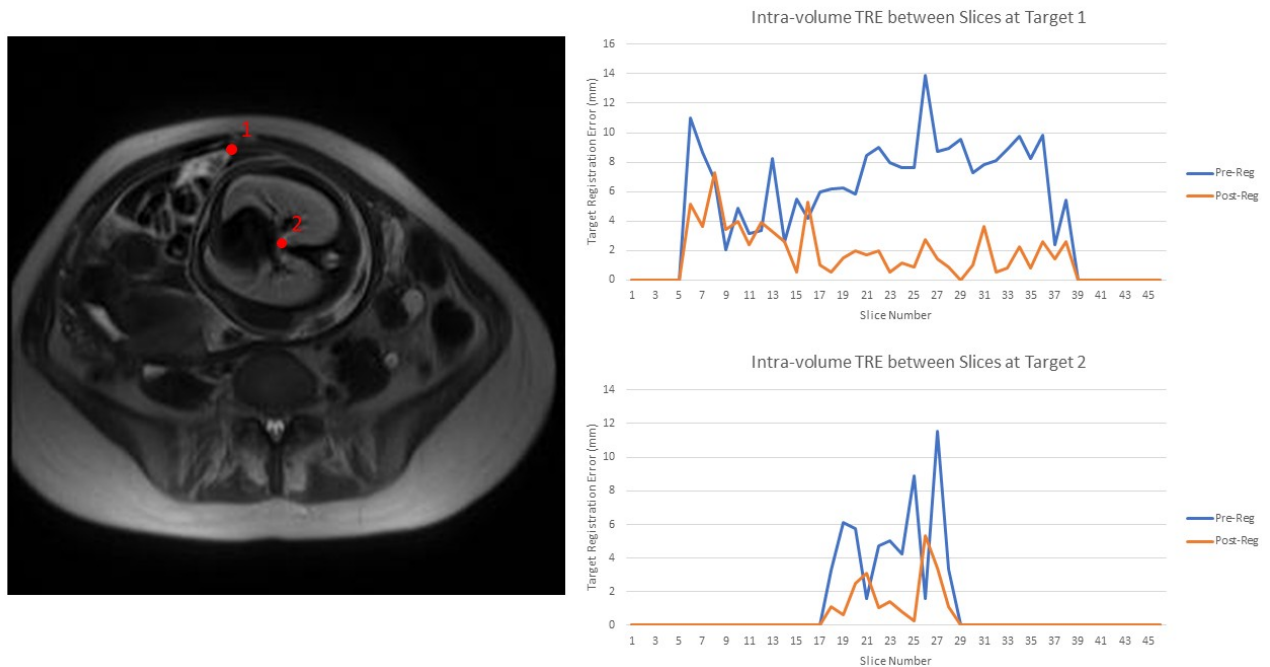


**Figure 13.** TRE plots between markers at adjacent slices for two selected anatomical landmarks, Target 1 and Target 2, across an MR image volume (left) before registration (blue lines) and after registration (orange lines).

## **3.4 DISCUSSION AND CONCLUSIONS**

### **3.4.1 Discussion**

There remains to be a reliable, widely accepted evaluation metric for assessing the accuracy and quantification of image quality improvement in intra-image registration. Whereas TRE is useful in analyzing registration performance in time sequences such as discrete contrast-enhanced MRI, there is no such one-to-one correspondence of points when comparing different slices within the same volume. Therefore, our intra-volume TRE results for one patient case may not be reflective of the same level of alignment improvement across all cases. However, in our studies, with side-by-side comparisons pre- and post-registration of simple visual inspections of the sagittal cross sections, as well as video play-throughs of the volume, we did not see any noticeable corruption of the original image, only improvements or minimal change in boundary alignments between slices.

### **3.4.2 Conclusions**

In this study, we presented a novel deformable registration technique for correcting motion artifacts in adjacent slices of prenatal abdominal MR images using the demons registration algorithm on interpolated sub-volumes. The algorithm preserves as much of the original placental and uterine structure as possible by only registering half of the interleaved slices and steers away from using the mid-space between images for calculating displacement vectors. Our MR image volume realignment pipeline is iterative and intuitive and does not require large amounts of data as deep-learning based solutions do. The results have been promising in aligning prenatal MR images with respiration artifacts, especially in cases where

the degree of motion between image acquisitions is very severe. In a future work, we plan to re-evaluate the registration algorithm used, perform a more quantitative analysis on registration results and generated DVFs, and further refine the image processing pipeline to create smooth and accurate placenta and uterine cavity MR images.

**CHAPTER 4**

**TOPOGRAPHY-BASED FEATURE EXTRACTION OF THE HUMAN PLACENTA**

**FROM PRENATAL MAGNETIC RESONANCE IMAGES**

**ABSTRACT**

Magnetic resonance imaging (MRI) has gained popularity in the field of prenatal imaging due to the ability to provide high quality images of soft tissue. In this study, we presented a novel method for extracting different textural and morphological features of the placenta from MRI volumes using topographical mapping.

**4.1 INTRODUCTION**

The current gold standard techniques for placental assessment are two-dimensional (2D) and three-dimensional (3D) ultrasound (US). However, conventional ultrasound imaging imposes several limitations on the physician, such as the lack of clear approximation of placental shape due to a small field of view and localization of features [12]. Recent studies have shown that magnetic resonance imaging (MRI) could provide additional information that can be used for easier and more accurate diagnosis of placental disorders [9] [52] [38]. MRI can potentially make up for the limitations of ultrasound by providing useful 3D information of placental, uterine, and fetal features with high soft-tissue contrast. These derived features can be further harnessed in computer-assisted magnetic resonance (MR) image analysis for placental abnormality detection [61] [62].

Topographic analysis is a technique commonly used in geoscience to study the surface properties of a land to characterize the land in many different ways. The extracted features (e.g., elevation data, complex spatial relationships between objects, etc.) are usually mapped on 2D plots from a bird's eye view with latitude data as one axis and longitude data as the other axis. The value of each feature of interest for each point is plotted with a corresponding color or intensity. In this study, our objective was to adopt a similar approach to analyze the structural, morphological, and textural characteristics of the placenta in MRI from a unique point of observation. To accomplish this, we proposed polar and planar topographical mapping methods to produce standardized 2D images of the placenta surface. The features extracted from the images included the entire placenta surface, as well as the thickness, intensity, and entropy maps displayed in a convenient two-dimensional format. The topography-based images may be useful for clinical placental assessments as well as computer-assisted diagnosis, and prediction of potential pregnancy complications with higher accuracy. This chapter encompasses our topography-based feature extraction and mapping methodologies and leaves the hypothesis testing for our future work on the deep-learning based fully automatic approaches for placenta abnormality diagnosis.

## **4.2 METHODS AND MATERIALS**

### **4.2.1 Data**

The data used in this topography study were the 241 T2-weighted registered axial MR image volumes as described following the registration procedure in Chapter 3. Before generating the topography maps, the image volumes were up-sampled using 3D cubic interpolation along the axial axis to ensure a smooth surface. To normalize the physical size of the voxels, the target

shape for interpolation was constructed as a mesh grid with spacing along the transverse (imaging) axis set to the same physical size of the voxels along the coronal and sagittal axes. The binary placenta and uterine cavity label volumes were up-sampled to the same size using level-set cubic interpolation [63].

#### 4.2.2 Polar topographic mapping

To initiate the topography-based feature extraction and mapping, we defined a fixed polar origin (PO). For this study, we selected a PO that was close to the center of mass of the uterine cavity while not being too close or distant from the placenta so as to generate clean, readable topography maps. The appointed standard for the PO was given as one and one-third times the distance vector from the placenta center of mass, or centroid, to the uterine cavity centroid, starting at the placenta centroid. A visualization of the choice of PO location is detailed in Figure 14. After establishing the new PO, a set of feature values was extracted from each surface point in the placenta label volume. We converted the placenta label volume to a surface with a thickness of one pixel. Each surface point of the placenta label was mapped to a new polar coordinate, defined using azimuth ( $\varphi$ ) and elevation ( $\theta$ ) angles. The azimuth angle ranged from -180 degrees to 180 degrees and the elevation angles ranged from -90 degrees to 90 degrees, creating a complete spherical view (see Figure 14). In this study, we scanned the surface of the placenta with a one-degree step size for both azimuth and elevation angles and extracted the distance, intensity, patch-based local average of intensities, local standard deviation of intensities, and local entropy of intensities as features from the contact points of each extruding ray from the PO. The rays, intuitively, had at least two points of contact with the placenta surface volume, one when entering the placenta and the second while exiting. We generated two separate

topography mappings for each image, one for the inner, or fetal surface closest to the PO, and the other for the outer, or maternal surface furthest from the PO. Figure 1c shows the two surfaces in relation to the PO location.

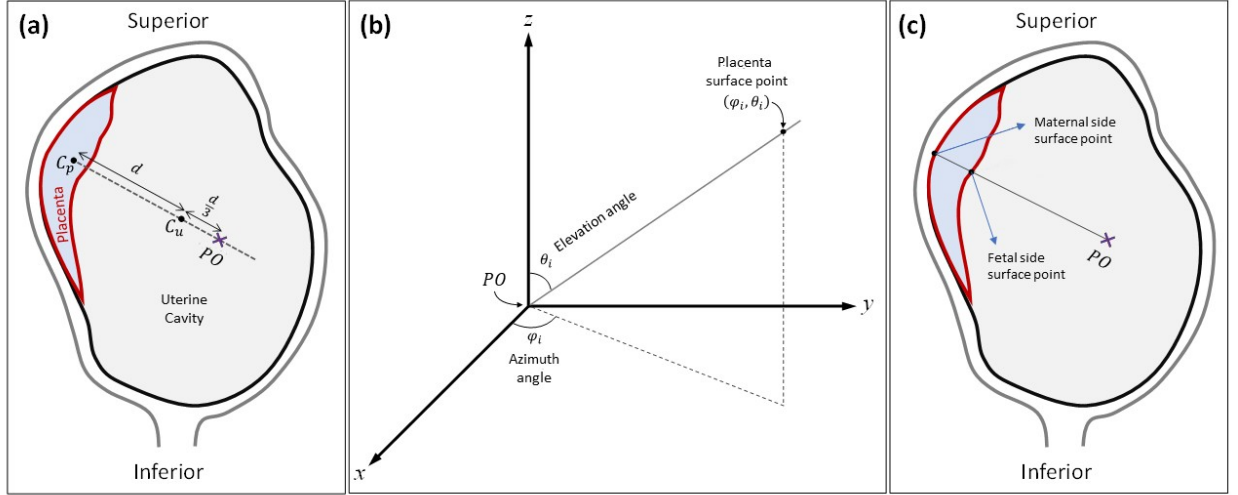


**Figure 14.** Polar topographic analysis approach. (a) Definition of PO location.  $C_p$  and  $C_u$  represent the centroid of the placenta and the uterine cavity, respectively. (b) Polar coordinate system used for topographic mapping.  $\phi_i$  and  $\theta_i$  are the azimuth angle and elevation angle of a given placenta surface point, respectively. (c) Definition of fetal and maternal side surfaces based on location of polar origin.

The azimuth and elevation angles were plotted on the x- and y- axes, respectively, to create a two-dimensional (2D) topography image of size 361 x 181 pixels, as shown in Figure 15. For inter-subject comparability of the topography maps, we normalized the placenta map by centering the centroid of the placenta. In this study, we extracted a total of eleven different feature maps per image volume as follows: *Distance (Fetal and maternal)*: the distance of the placenta surface points from the PO. This reflects some topological characteristics of the



placenta. *Placenta thickness*: the difference between the maternal side distances from the fetal side distances. *Surface intensity (Fetal and maternal)*: the intensity of the image at the surface points. *Local average of intensities (Fetal and maternal)*: the average of patch-based intensities, using patches of size  $11 \times 11 \times 11 \text{ mm}^3$  centered at each surface point. This is less affected by artifacts and noise observed on surface intensity maps. *Local standard deviation of intensities (Fetal and maternal)*: the standard deviation of patch-based intensities, using patches of size  $11 \times 11 \times 11 \text{ mm}^3$  centered at each surface point. *Local entropy of intensities (Fetal and maternal)*: the entropy of patch-based intensities, using patches of size  $11 \times 11 \times 11 \text{ mm}^3$  centered at each surface point.

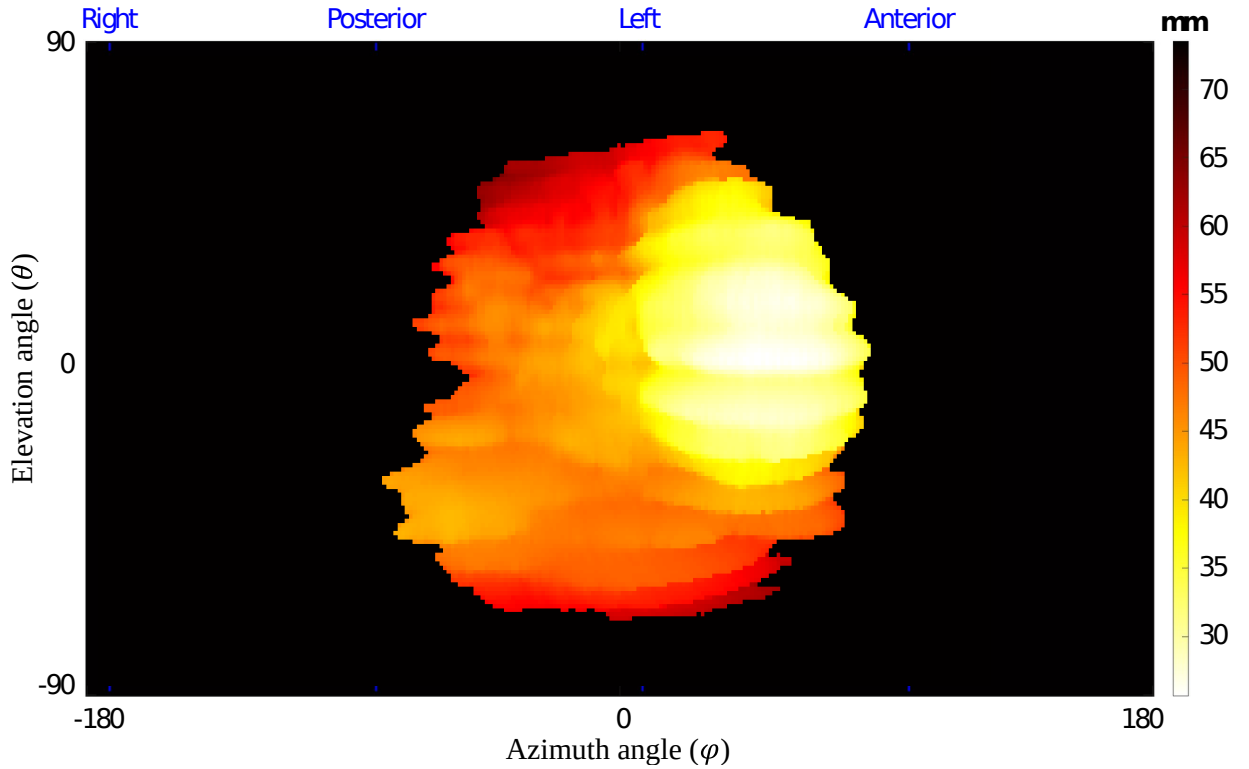
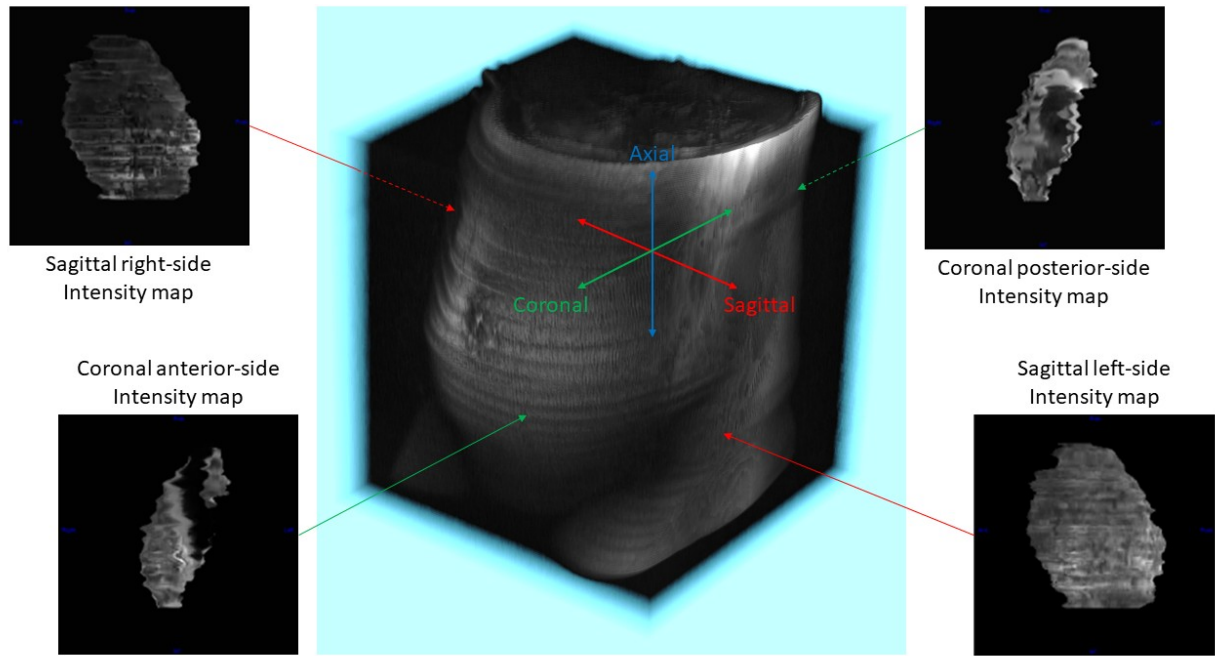


**Figure 15.** A topographic distance map for the maternal side surface points in a sample case. The dashed lines show the anterior, posterior, right, and left orientations based on

the MR imaging axes. The top and bottom of the topography map show the superior and inferior sides, respectively.

#### **4.2.3 Planar topographic mapping**

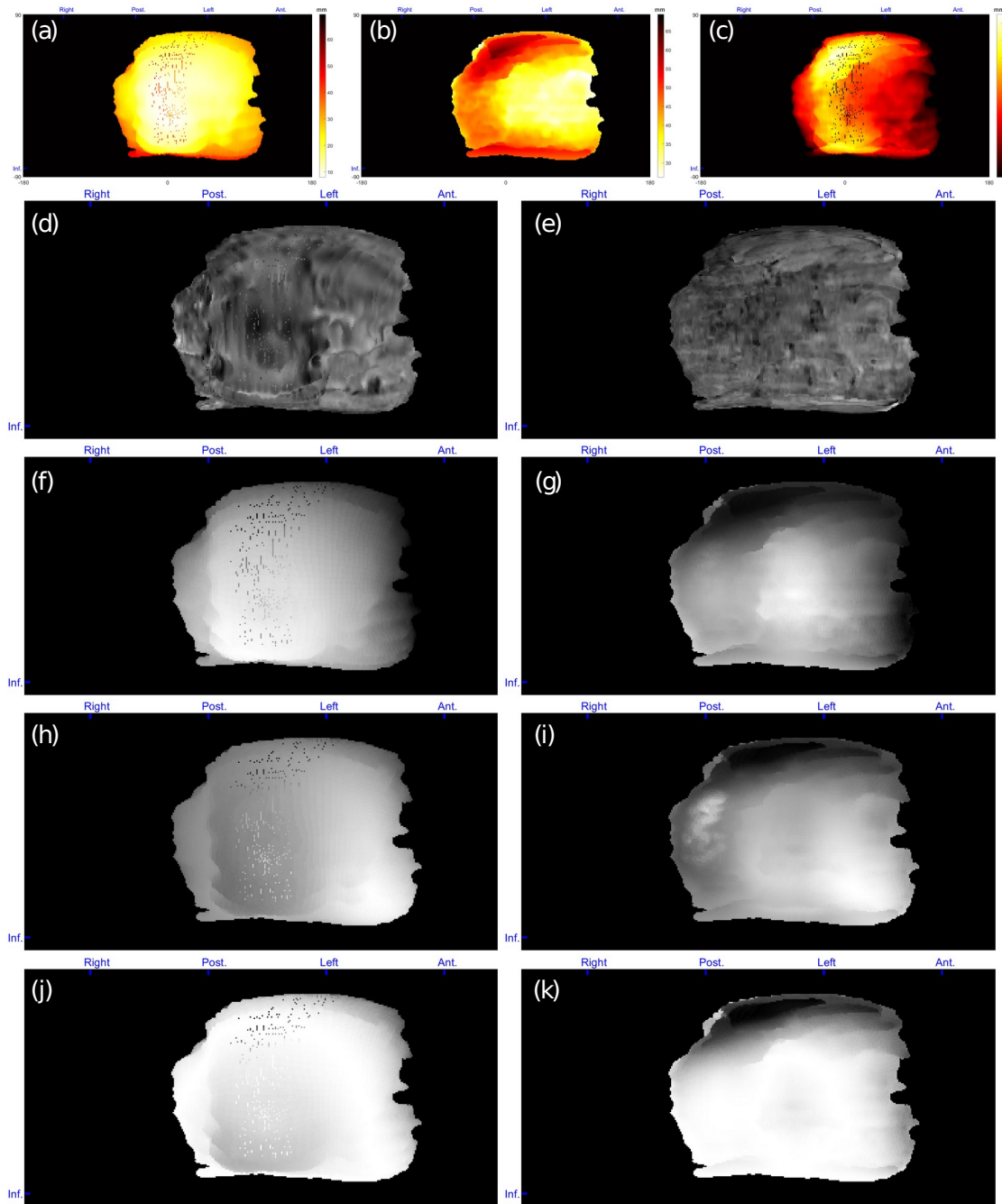
In addition to the polar topographic mapping methodology, we implemented a planar topographic mapping. This method involved taking the placenta surface feature maps as viewed from the sagittal left-side plane and the coronal anterior-side plane of the MR image volume. The MR image volume and placenta label volume were first centered based on the placenta center of mass. Similar to the polar topographic mapping method, the placenta label was converted to a surface map with a thickness of one pixel. In contrast with the polar topographic mapping method which can be thought of as casting rays outwards from a set singular point, the planar topographic mapping casts parallel rays at each pixel location across the image. Parallel rays were cast from each point on the sagittal left-side plane and coronal anterior-side plane of the image volume and four separate topography mappings were generated, one for each placental surface closest to the sagittal left- and right-side and coronal anterior- and posterior-side planes (see Figure 16). The coronal and sagittal distance maps were calculated referencing the coronal and sagittal planes intersecting the uterine cavity center of mass, respectively. For each surface point, the same features detailed in the polar topographic mapping section were extracted, which totaled to twenty-two different feature maps per image volume when including thickness.



**Figure 16.** Planar topographic mapping definitions and sample intensity maps. The four surfaces extracted and featurized were the sagittal left- and right-side and the coronal anterior- and posterior-side surfaces. Sample feature maps shown are intensity maps taken from each of the four surfaces.

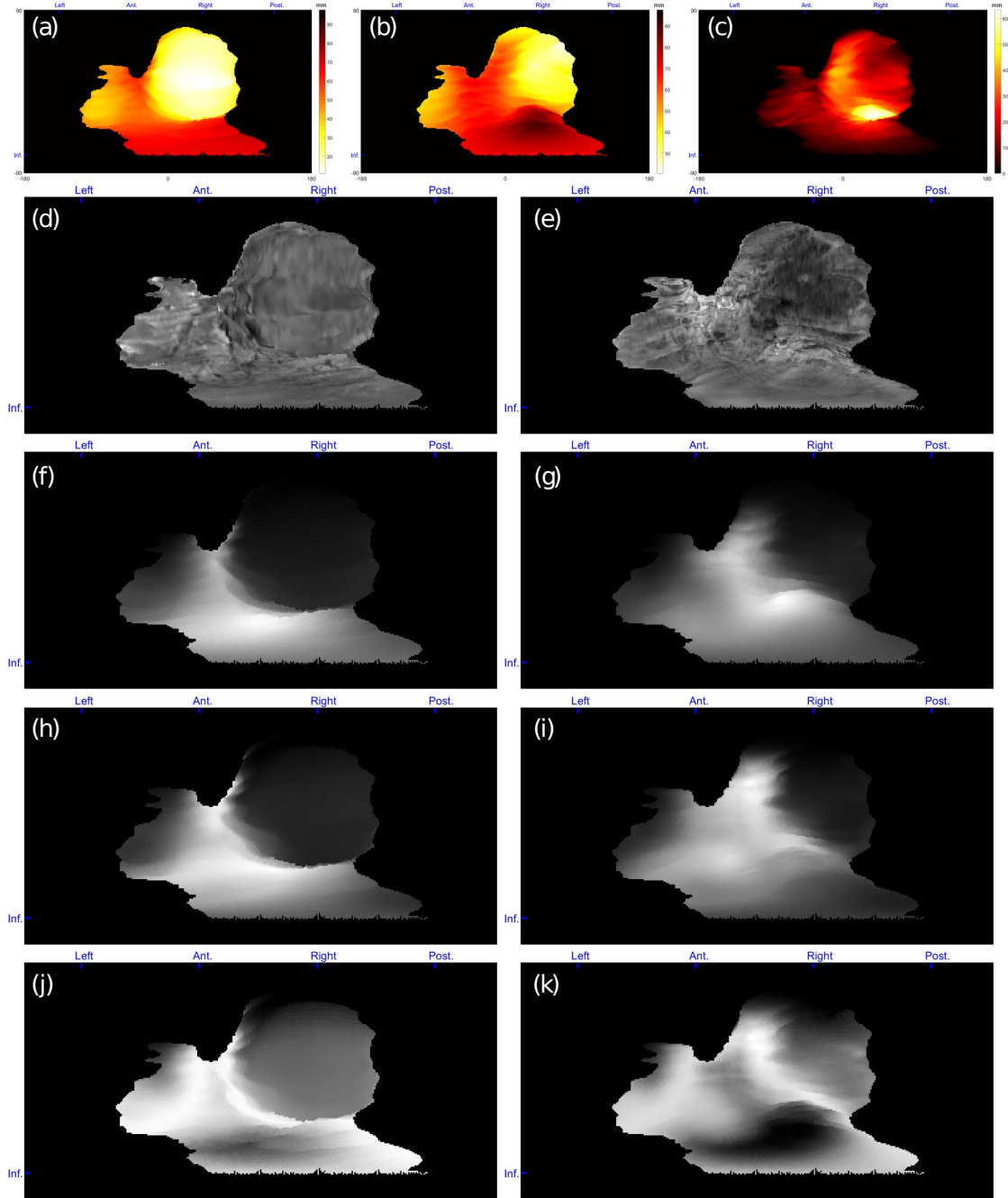
### 4.3 RESULTS

Figure 17 shows the extracted polar topography-based features for a normal case. Figure 18 shows the polar topography-based features extracted from a prenatal MRI of a PAS suspected pregnant woman with postpartum hysterectomy. Figure 19 shows the extracted planar topography-based features for another normal case.



**Figure 17.** Polar topographic feature maps from a normal case. Given as a) distance of placenta fetal side from POV, b) distance of placenta maternal side from POV, c) placenta thickness, d) intensity of placenta fetal side, e) intensity of placenta maternal side, f) local average intensity of placenta fetal side, g) local average intensity of

placenta maternal side, h) local intensity STD of placenta fetal side, i) local intensity STD of placenta maternal side, j) local entropy of placenta fetal side, and k) local entropy of placenta maternal side. For patch-based feature extraction.



**Figure 18.** Polar topographic feature maps from a PAS suspected case with postpartum hysterectomy. Given as a) distance of placenta fetal side from POV, b) distance of placenta maternal side from POV, c) placenta thickness, d) intensity of placenta fetal side, e) intensity of placenta maternal side, f) local average intensity of placenta fetal side, g) local average intensity of placenta maternal side, h) local intensity STD of placenta fetal side, i) local intensity STD of placenta maternal side, j) local entropy of placenta fetal side, and k) local entropy of placenta maternal side. For patch-based feature extraction.

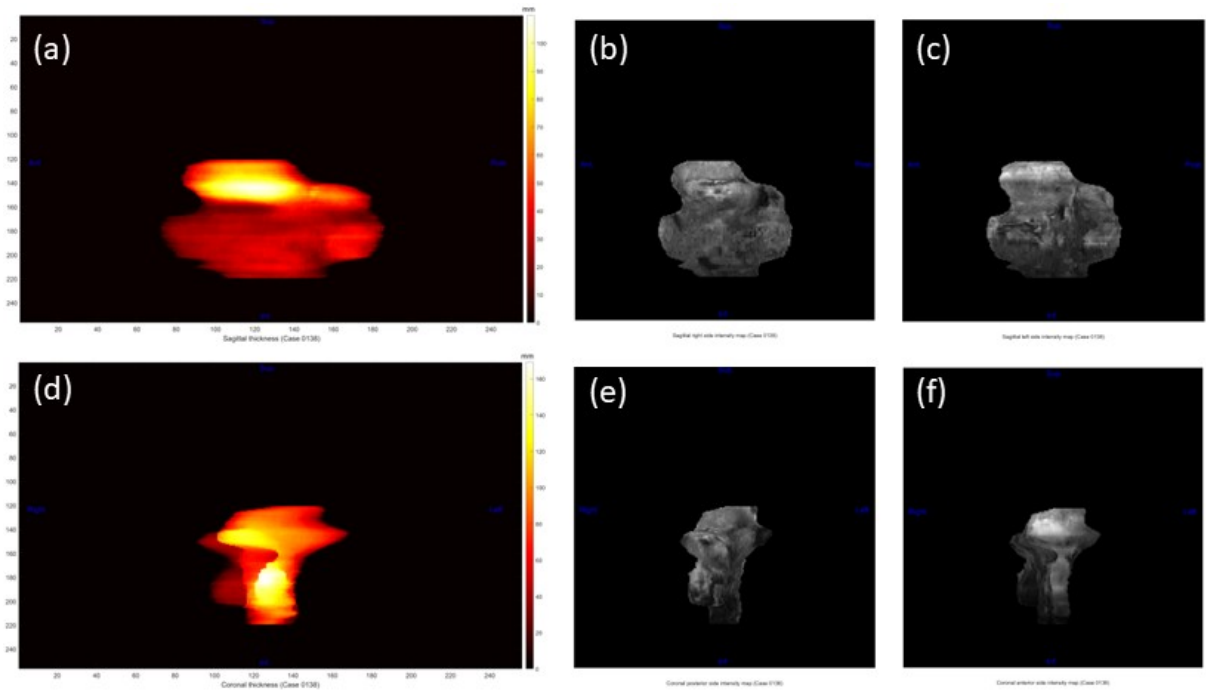


**Figure 19.** Planar topographic feature maps from a normal case. For the sagittal plane, a) is the thickness map, b) is the left-side intensity map, and c) is the right-side intensity map. For the coronal plane, d) is the thickness map, e) is the posterior-side intensity map, and f) is the anterior-side intensity map.

## 4.4 DISCUSSION AND CONCLUSIONS

### 4.4.1 Discussion

One limitation of this study is the movement of body and/or fetus during the relatively long MR imaging time. These misalignments movements cause some imaging artifacts that could be reflected on the maps, as shown in Figure 20a. Although smoothing of the surface following the registration in step in Chapter 3 was found to reduce the severity of visible artifacts in the constructed topography maps, they were not entirely eliminated. In addition, if the placenta is extended toward the inferior or superior sides of the uterus, an artifact is observed in polar topographic mapping because of the fewer number of placenta surface voxels with the elevation angles close to  $-90$  and  $90$  degrees. Figure 20b-c shows two samples of this kind of artifact. This issue could be addressed by interpolating the maps at the regions with missing topographic data.

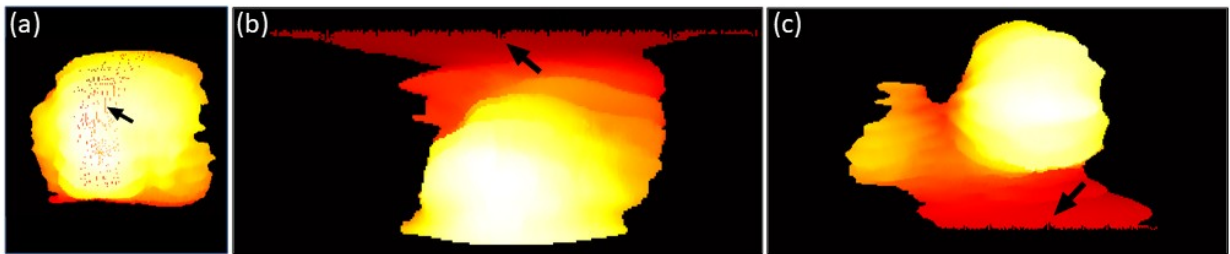


**Figure 20.** Artifacts of the polar topography mapping. A) Effect of intra-volume slice misalignment on the topography map. Mapping artifacts at the b) superior and c) inferior sides of the placenta for two sample cases.

On the other hand, the planar topographical mapping method does not suffer from the edge effects observed in Figure 20b-c, but do not provide the singular 360-degree field of view of the placenta that the polar method does. It is currently unclear which method provides more useful features, as here we have only presented the image processing steps without quantitative analysis on the data.

#### **4.4.2 Conclusions**

We proposed a topographical feature extraction and mapping approach for MR image volumes of pregnancies. Through this new technique, we aim to help analyze the images from a new point of observation. The extracted features could be useful for the detection of certain placental disorders and better prediction of life-threatening postpartum complications when combined with computational algorithms. As a future work, we are going to use the results of this work in a retrospective study on a deep learning-based classification for PAS detection and postpartum hysterectomy prediction, which should elucidate certain tradeoffs between the two methods for placental topography mapping detailed in this chapter.



## CHAPTER 5

### CONCLUSIONS AND FUTURE DIRECTIONS

#### 5.1 CONCLUSIONS

This thesis work has established a pipeline for fast and automatic segmentation, registration, and feature extraction for placental MR images of pregnant women.

In Chapter 2, we proposed a deep learning neural network for automatic segmentation of the placenta and uterine cavity from MR images. We achieved an improvement in dice score on the segmentation of the placenta and uterine cavity with no tradeoffs in terms of processing time. A current literature review suggests that our model, with a DSC of 87.7% for the placental segmentation on sagittal T2-weighted MRI and a DSC of 95.3% on the uterine cavity segmentation, is state-of-the-art. In addition, to our knowledge, this is the first implementation of the U-Net 3+ architecture in three dimensions, although training such a model on entire image volumes is still quite challenging with memory limitations.

In Chapter 3, we applied the demons registration algorithm in a new way to present a solution for the abdominal MRI interleaved acquisition misalignment problem. Our methods do not rely on the mid-space between images, which allows for intra-image deformable registration to occur with minimal disruptions to the original shape of structures in the image. Mid-space independent registration has been the subject of a few studies within the past few years but has never been applied to intra-image registration in this capacity.

In Chapter 4, we presented a novel approach for extracting features from the placenta in MR images that can be utilized in future studies for computer-assisted diagnosis of placental

abnormal conditions and hysterectomy prediction algorithms. To the best of our knowledge, this is the first time that a topographic analysis has been used for placenta MRI.

In addition to introducing a new perspective for visualizing the placenta surface and structure, we have proposed a neural network for fully automatic segmentation of the placenta and uterine cavity from prenatal MRI and confronted a salient issue in abdominal MRI through a new registration technique. Our 3D U-Net 3+ model for automatic placenta and uterine cavity label predictions achieved state-of-the-art (SOTA) performance on the sagittal MRI dataset and performed similarly to current SOTA models on the axial MRI dataset. We believe that our segmentation model can be easily applied to other abdominal MRI segmentation applications, such as the delineation of the kidneys or liver for diagnosing tumors. The registration study for MR image alignment and the topography study for placental surface feature extraction have also shown promising results. Our proposed registration methods could potentially see success in the analysis of other soft tissue structures in the human body, including the liver. We believe that the topographical extraction approach we used for the placenta could be adopted for other imaging modalities and for different organs.

## **5.2 DISCUSSIONS**

The current limitations on the proposed methods in this thesis work are associated with the accuracy of the placenta and uterine segmentation network, the evaluation metrics for registration performance, and the artifacts in the placenta topography maps. Segmentation performance on the axial dataset, which included patients who underwent postpartum hysterectomy, was noticeably lower than on the sagittal dataset with only normal cases despite

having more data points for training and testing. This disparity in performance may have been attributed to by a few factors, such as inherent advantages of sagittal MRI for prenatal imaging over axial MRI due to placenta locale and orientation in the body or wide variations in placenta structure in cases of placental disorders. Other limitations of the segmentation study in Chapter 2 included the memory issues and amount of data for training. A larger memory cache would allow for larger block inputs, providing more feature information to the network and potentially improving segmentation results.

The evaluation of the registration methodologies presented in Chapter 3 for interleaved MRI alignment are still quite preliminary, with primarily visual results of cross sections and 3D surfaces of registered labels for a few sample cases. The registration study would benefit from introducing a more reliable quantitative evaluation metric for determining registration performance which will require a further investigation into abdominal MRI registration literature. Although the topographical mapping methods in Chapter 4 did see a reduction in noise, holes, and other artifacts as a result of the registration step, the issues still remain at a lesser degree. Additionally, in cases where the placenta is greatly extended towards the superior or inferior ends of the uterine cavity, the topography map lacks data points near the edge of the placenta, creating a wave-like artifact.

### **5.3 FUTURE DIRECTIONS**

Although out of the scope of this thesis work, we plan to employ the generated topographical maps in a deep learning-based classification model for predicting hysterectomies

and other postpartum complications from prenatal MRI. This approach is focused on the features that are related to the placenta topology as well as local superficial imaging pattern and texture of the placenta in MR images. Our preliminary observations confirmed that using the topography-based feature maps could be useful in improving the performance on the computer-assisted algorithms used for automatic detection of PAS and prediction of postpartum hysterectomy. In a future work, we will also investigate the tradeoffs between sagittal and axial MRI for prenatal imaging from a computer-assisted diagnosis perspective. To make the tools presented in this thesis work useful in a clinical setting, we will have to further improve the segmentation performance, especially for abnormal placentation cases, as well as develop a method for detecting placenta complications from the generated topography maps and features. The proposed topography methods would also benefit from an interpolation step near the superior and anterior borders of the placenta to compensate for missing points at those locations. This holistic image analysis and feature extraction approach could be also adopted for other 2D or 3D imaging modalities and for different organs. We will be continuing to strive towards creating a fast and reliable system for diagnosis of placental disorders from prenatal MRI.

## BIBLIOGRAPHY

- [1] M. Costa et al., "The endocrine function of human placenta: an overview," *Reproductive BioMedicine Online*, vol. 32, no. 1, pp. 14-43, 2016.
- [2] N. Gude et al., "Growth and function of the normal human placenta," *Thrombosis Research*, vol. 114, no. 5-6, pp. 397-407, 2004.
- [3] E. Norwitz and R. Errol, "Defective implantation and placentation: laying the blueprint for pregnancy," *Reprod Biomed Online*, vol. 13, no. 4, pp. 591-599, 2006.
- [4] I. Brosens et al., "The "Great Obstetrical Syndromes" are associated with disorders of deep placentation," *Am. J. Obstet. Gynecol.*, vol. 204, no. 3, pp. 193-201, 2011.
- [5] S. Rees, R. Harding and D. Walker, "Fetal and neonatal origins of altered brain development," *Early Hum Dev*, vol. 81, no. 5, pp. 753-761, 2005.
- [6] A. Guttmacher et al., "The Human Placenta Project: Placental structure, development, and function in," *Placenta*, vol. 35, no. 5, pp. 303-304, 2014.
- [7] R. Silver and D. W. Branch, "Placenta Accreta Spectrum," *N Engl J Med*, vol. 378, no. 16, p. 1529:1536, 2018.
- [8] J. Leyendecker et al., "MRI of pregnancy-related issues: abnormal placentation," *Am. J. Roent.*, vol. 198, no. 2, pp. 311-320, 2012.
- [9] C. Maldjian et al., "MRI appearance of placenta percreta and placenta accreta," *Magnetic resonance imaging*, vol. 17, no. 7, pp. 965-971, 1999.
- [10] E. Hafner et al., "Second-trimester measurements of placental volume by three-dimensional ultrasound to predict small-for-gestational-age infants," *Ultraousound Obstetr. Gynecol.*, vol. 12, pp. 97-102, 1998.
- [11] J. Hasegawa et al., "Placenta volume measurement in clinical practice," *J. Ultrasound Obstet. Gynecol.*, vol. 9, pp. 408-412, 2015.
- [12] P. Switzer, C. James and M. Frettag, "Value and limitations of obstetrical ultrasound: uncovering abnormalities at earlier stages," *Canadian Family Physician*, vol. 38, p. 121, 1992.

- [13] P. McGinty et al., "Ultrasound assessment of placental function: effectiveness of placental biometry in a low-risk population as a predictor of a small for gestational age neonate," *Prenatal Diagnosis*, vol. 32, pp. 620-626, 2012.
- [14] L. Merce et al., "Intervillous and uteroplacental circulation in normal early pregnancy and early pregnancy loss assessed by 3-dimensional power Doppler angiography," *Am J Obstet Gynecol*, vol. 200, no. 3, p. 315, 2009.
- [15] J. Alcazar, "Three-dimensional power Doppler derived vascular indices: what are we measuring and how are we doing it?," *Ultrasound Obstet Gynecol*, vol. 32, no. 4, pp. 485-487, 2008.
- [16] N. Andescavage, A. Plessis and C. Limperopoulos, "Advanced MR imaging of the placenta: exploring the in utero placenta-brain connection," *Seminars in Perinatology*, vol. 39, no. 2, pp. 113-123, 2015.
- [17] S. Dekan et al., "MRI of the placenta - a short review," *Wiener Medizinische Wochenschrift*, vol. 162, no. 9, pp. 225-228, 2012.
- [18] D. Levine, P. Barnes and R. Edelman, "Obstetric MR imaging," *Radiology*, vol. 211, no. 3, pp. 609-617, 1999.
- [19] B. Allen and J. Leyendecker, "Placental evaluation with magnetic resonance," *Radiol Clin North Am*, vol. 51, no. 6, pp. 955-966, 2013.
- [20] M. Han et al., "Automatic segmentation of human placenta images with U-Net," *IEEE Access*, vol. 7, pp. 180083-180092, 2019.
- [21] M. Shahedi et al., "Segmentation of uterus and placenta in MR images using a fully convolutional neural network," *Medical Imaging 2020: Computer-Aided Diagnosis*, vol. 11314, pp. 411-418, 2020.
- [22] M. Shahedi et al., "Deep learning-based segmentation of the placenta and uterus on MR images," *Journal of Medical Imaging*, vol. 8, no. 5, p. 054001, 2021.
- [23] M. Shahedi et al., "Automatic segmentation of uterine cavity and placenta on MR Images using deep," *Medical Imaging 2022: Biomedical Applications in Molecular, Structural, and Functional Imaging*, vol. 12036, pp. 287-293, 2022.
- [24] P. Looney et al., "Fully automated 3-D ultrasound segmentation of the placenta, amniotic fluid, and fetus for early pregnancy assessment," *IEEE Transactions on Ultrasonics, Ferroelectrics, and Frequency Control*, vol. 68, no. 6, pp. 2038-2047, 2021.

- [25] R. Hu et al., "Automated placenta segmentation with a convolutional neural network weighted by acoustic shadow detection," *2019 41st Annual International Conference of the IEEE Engineering in Medicine and Biology Society*, vol. 2019, pp. 6718-6723, 2019.
- [26] A. Alansary et al., "Fast fully automatic segmentation fo the human placenta from motion corrupted MRI," *International conference on medical image computing and computer-assisted intervention*, vol. 2016, pp. 589-597, 2016.
- [27] G. Wang et al., "Slic-Seg: A minimally interactive segmentation of the placenta from sparse and motion-corrupted fetal MRI in multiple views," *Medical Image Analysis*, vol. 34, no. 1, pp. 137-147, 2016.
- [28] G. Wang et al., "DeepIGeoS: A deep interactive geodesic framework for medical image segmentation," *IEEE Transactions on Pattern Analysis and Machine Intelligence*, vol. 41, no. 7, pp. 1559-1572, 2018.
- [29] Z. Zhang et al., "Multi-region saliency-aware learning for cross-domain placenta image segmentation," *Pattern Recognition Letters*, vol. 140, pp. 165-171, 2020.
- [30] V. Zimmer et al., "Placenta segmentation in ultrasound imaging: Addressing sources of uncertainty and limited field-of-view," *arXiv*, vol. 2206, no. 14746, 2022.
- [31] A. Uus et al., "Deformable slice-to-volume registration for motion correction of fetal body and placenta MRI," *IEEE Transactions On Medical Imaging*, vol. 39, no. 9, pp. 2750-59, 2020.
- [32] J. Guyader et al., "Influence of image registration on apparent diffusion coefficient images computed from free-breathing diffusion MR images of the abdomen," *Journal of Magnetic Resonance Imaging*, vol. 42, no. 2, pp. 315-330, 2014.
- [33] A. Menys et al., "Dual registration of abdominal motion for motility assessment in free-breathing data sets acquired using dynamic MRI," *Physics in Medicine and Biology*, vol. 59, no. 16, p. 4603, 2014.
- [34] Q. Chang et al., "An unsupervised 3D recurrent neural network for slice misalignment correction in cardiac MR imaging," *International Workshop on Statistical Atlases and Computational Models of the Heart*, vol. 2021, pp. 141-150, 2021.
- [35] M. Staudt et al., "Right-hemispheric organization of language following early left-sided brain lesions: function MRI topography," *NeuroImage*, vol. 16, pp. 954-967, 2002.

- [36] Z. Cohen et al., "Knee cartilage topography, thickness, and contact areas from MRI: in-vitro calibration and in-vivo measurements," *Osteoarthritis and Cartilage*, vol. 7, pp. 95-109, 1999.
- [37] P. Lim et al., "Utility of ultrasound and MRI in prenatal diagnosis of placenta accreta: a pilot study," *AJR*, vol. 197, no. 6, p. 1506, 2011.
- [38] A. Derman et al., "MRI of placenta accreta: a new imaging perspective," *AJR*, vol. 197, no. 6, pp. 1514-21, 2011.
- [39] R. Namias et al., "Uterus segmentation in dynamic MRI using LBP texture descriptors,," *SPIE Medical Imaging*, vol. 9034, no. 1, p. 90343W, 2014.
- [40] M. Hesamian et al., "Deep learning techniques for medical image segmentation: achievements and challenges," *Journal of Digital Imaging*, vol. 32, no. 1, pp. 582-596, 2019.
- [41] H. Huang et al., "UNet 3+: A full-scale connected UNet for medical image segmentation," *IEEE International Conference on Acoustics, Speech and Signal Processing (ICASSP)*, vol. 2020, pp. 1055-1059, 2020.
- [42] P. Furtado, "Improving deep segmentation of abdominal organs MRI by post-processing," *Biomedinformatics*, vol. 1, pp. 88-105, 2021.
- [43] D. Huttenlocher, G. Klanderman and W. Rucklidge, "Comparing images using the Hausdorff distance," *IEEE Transactions on pattern analysis and machine intelligence*, vol. 15, no. 9, pp. 850-863, 1993.
- [44] R. Semelka, M. Brown and E. Altun, *Abdominal-pelvic MRI*, John Wiley & Sons, 2015.
- [45] S. Keller et al., "Image artifacts from MR-based attenuation correction in clinical, whole-body PET/MRI," *Magnetic Resonance Materials in Physics, Biology and Medicine*, vol. 26, no. 1, pp. 173-181, 2013.
- [46] M. Bernstein, K. King and X. Zhou, *Handbook of MRI pulse sequences*, Burlington, MA: The British Institute of Radiology, 2004.
- [47] Y. Guo et al., "Improved IVIM MRI of small lesions in the liver by deformable image registration," *Annual Meeting & Exhibition of the International Society for Magnetic Resonance in Medicine*, 2016.
- [48] I. Aganj et al., "Mid-space-independent deformable image registration," *Neuroimage*, vol. 152, pp. 158-170, 2017.



- [49] D. Yang et al., "A fast inverse consistent deformable image registration method based on symmetric optical flow computation," *Physics in Medicine and Biology*, vol. 53, no. 21, pp. 6143-65, 2008.
- [50] O. Skrinjar, A. Bistoquet and H. Tagare, "Symmetric and transitive registration of image sequences," *Int J Biomed Imaging*, p. 686875, 2008.
- [51] B. Avants and J. Gee, "Geodesic estimation for large deformation anatomical shape averaging and interpolation," *Neuroimage*, vol. 23, pp. S139-50, 2004.
- [52] A. Kilcoyne et al., "MRI of placenta accreta, placenta increta, and placenta percreta: pearls and pitfalls," *Am. J. Roent.*, vol. 208, no. 1, pp. 214-221, 2017.
- [53] K. Murphy et al., "Evaluation of registration methods on thoracic CT: The EMPIRE10 challenge," *IEEE Transactions on Medical Imaging*, vol. 30, no. 11, pp. 1901-20, 2011.
- [54] J. Thirion, "Image matching as a diffusion process: an analogy with Maxwell's demons," *Medical Image Analysis*, vol. 2, no. 3, pp. 243-260, 1998.
- [55] J. Thirion, "Non-rigid matching using demons," *Proceedings of IEEE CVPR96*, vol. 1, pp. 245-251, 1996.
- [56] J. Thirion, G. Subsol and D. Dean, "Cross validation of three inter-patients matching methods," *Visualization in Biomedical Computing*, vol. 1131, pp. 327-336, 1996.
- [57] H. Wang et al., "Validation of an accelerated 'demons' algorithm for deformable image registration in radiation therapy," *Physics in Medicine and Biology*, vol. 50, no. 12, pp. 2887-50, 2005.
- [58] X. Pennec, P. Cachier and N. Ayache, "Understanding the 'demon's algorithm': 3D non-rigid registration by gradient descent," *Medical Image Computing and Computer-Assisted Intervention, Miccai'99, Proceedings*, pp. 597-605, 1999.
- [59] X. Yang et al., "Nonrigid registration and classification of the kidneys in 3D dynamic contrast enhanced (DCE) MR images," *Medical Imaging 2012: Image Processing*, vol. 8314, pp. 105-112, 2012.
- [60] P. Kostelec, J. Weaver and D. Healy Jr., "Multiresolution elastic image registration," *Medical Physics*, vol. 25, pp. 1593-604, 1998.
- [61] V. Romeo et al., "Machine learning analysis of MRI-derived texture features to predict placenta accreta," *Magnetic resonance imaging*, vol. 64, pp. 71-76, 2019.

- [62] Y. Ueno et al., "Novel MRI finding for diagnosis of invasive placenta praevia: evaluation of findings," *European radiology*, vol. 24, no. 4, pp. 881-888, 2014.
- [63] M. Salarian et al., "Toward quantitative digital histopathology for prostate cancer: comparison of inter-slide interpolation methods for tumour measurement," *Medical Imaging 2013: Digital Pathology*, vol. 8676, pp. 146-151, 2013.
- [64] G. Burton and E. Jauniaux, "What is the placenta?," *American Journal of Obstetrics and Gynecology*, vol. 213, no. 4, pp. S6.e1-S6.e4, October 2015.
- [65] M. Turco and A. Moffett, "Development of the human placenta," *Development*, vol. 146, no. 22, p. dev163428, 2019.
- [66] P. Beddy et al., "Magnetic resonance imaging for the evaluation of acute abdominal pain in pregnancy," *Seminars in Ultrasound, CT, and MRI*, vol. 31, no. 5, pp. 443-441, 2010.
- [67] G. Masselli et al., "Acute abdominal and pelvic pain in pregnancy: ESUR recommendations," *European radiology*, vol. 23, no. 12, pp. 3485-3500, 2013.

## **BIOGRAPHICAL SKETCH**

## **CURRICULUM VITAE**